공학박사학위논문

Multiscale Design and Fabrication of Polymeric Architectures for Wettability Control and Fuel Cell Applications

멀티스케일 고분자 구조물 설계 및 제작을 통한 젖음 특성 조절 및 연료전지 응용

2015 년 2 월

서울대학교 대학원

기계항공공학부

김 상 문

Abstract

In this thesis, we describe novel and facile methods to achieve multiscale, asymmetric structures via controlled oxygen-inhibition effect of UV-curable materials and guided UV light transmission. From the nature-inspired multiscale structures with the aid of thermally responsive chemical composition, we could exhibit directional liquid control in microfluidic system and also achieve enhanced performance of polymer electrolyte membrane fuel cell.

First, we propose methodological breakthroughs to achieve multiscale structures mimicking biological surfaces in nature. Representatively, multiplex lithography via stacking designed polymeric membrane provides possibility for hierarchical design of pattern dimension at each layer and number of layers. The facile yet versatile strategy for multiscale structures from soft materials allows structural deformations on surface and enables LEGO® -like, monolithic integrations of them by quantitatively controlling the oxygen-inhibition effect of UV-curable materials. Micro ebb tides of partially cured resin were observed and utilized to form dual phase brick with viscoelastic coating that was promoted to be nanopatterns and connections under multiple UV exposures. Furthermore, to realize asymmetric ratchet structure in morphobutterfly wings or water strider legs, we developed a simple but powerful strategy to directly program asymmetric

structures within a microchannel by combination of photopolymerization within a microchannel and the guided light transmission through an optically asymmetric Lucius prism array.

Next, we present the asymmetric ratchet structures, created at the bottoms of microchannels, show the unidirectional liquid flows as well as controlling the fluid speed in a predefined region. Then, we demonstrated two examples of asymmetric structures created or programmed in specific regions within microchannels to control the fluid speed in predefined regions and to be used as on-chip timers in split microchannels. In addition, we present a simple approach to reversibly switch the direction of liquid flow on physically symmetric and chemically asymmetric prism structures by exploiting the reversibility of wetting properties on a thermo-responsive polymer, poly(N-isopropyl-acrylamide) surface is demonstrated. Such an asymmetric prism array creates a flow path in the direction of the lower critical contact angle. This allows a unidirectional “step flow” across the ridges of prism channels, which can be made reversible with suitable temperature change.

Finally, we demonstrate enhancing performance in polymer electrolyte membrane fuel cell (PEMFC) via multiscale approaches. To improve mass transport in cathode electrode, carbon-supported Pt (Pt/C) catalyst was selectively

functionalized by a thermally responsive poly(N-isopropylacrylamide) (PNIPAM) to improve water transport in the cathode of proton exchange membrane fuel cell. Amine-terminated PNIPAM selectively reacted with the functional group of –COOH on carbon surfaces of Pt/C via the amide reaction by 1-ethyl-3-(3-dimethylaminopropyl)carbodiimide (EDC) as a catalyst. Pt surfaces of Pt/C were intact throughout the carbon surface functionalization, and the carbon surface property could be thermally changed. The PNIPAM-functionalized Pt/C was well dispersed due to its hydrophilic surface property at room temperature during the catalyst ink preparation. In sharp contrast, when PEMFC was operated at 70 ℃, PNIPAM-coated carbon surface of Pt/C became hydrophobic, which resulted in a decrease in water flooding in the cathode electrode. Due to the switched wetting property of the carbon surface, PEMFC with PNIPAM-functionalized Pt/C catalyst in the cathode showed high performance in the high current density region. To explain the enhanced water transport, we proposed a simple index as the ratio of systematic pressure (driving force) and retention force. Furthermore, to demonstrate the effectiveness of multiscale engineering, complex and multiscale architectures with an aid of multiplex lithography that integrates rational advantages in both microscale and nanoscale, was embedded into fuel cell devices to fully probe advantages of each scale pattern, resulting in outstanding device performance by increasing both proton conductivity and surface area for electrocatalysis.

Key Words : Multiscale structures, Asymmetric structure, UV curable materials, Thermoresponsive polymer (poly(N-isopropylacrylamide)), Directional liquid flow, High performance polymer electrolyte membrane fuel cell.

Student Number: 2010-22782

Contents

List of Figures

array. (b) The control of liquid flow velocity by the ratchet orientation along with representative movie cuts. The graph demonstrates the change in liquid flow velocity on the programmed asymmetric structures. (Insets: a schematic of asymmetry of ratchets of different regions and microscopic pictures of interfaces)

Figure 3-5. An example showing the delayed fluid flow based on different ratchet structures created within a microchannel. (a) A schematic illustration on differently oriented ratchet structures in three different channel regions. (b) Movie cuts showing the delayed fluid flow induced by different ratchet structures. In good agreement with the previous experimental results of controlled liquid flow velocity, injected liquid sequentially reached the regions 1, 2, and 3 with time lapse.

Figure 3-6. (a) A schematic illustration for the fabrication of a two-face prism array. (b) SEM image of a prism array showing the symmetric structure in microscale. The inset shows a magnified SEM image of the prism array with chemical asymmetry. (c) An optical microscope image showing the left faces of the prisms are covered with metal films.

Figure 3-7. (a) Movie cuts at various times showing the unidirectional liquid step flow. The water front is moving unidirectionally toward the metal-free PNIPAAm surface (right face). It is noted that the black column on the liquid is a needle of the equipment for feeding water at a constant rate. The inset in each image shows the corresponding magnified image at the three-phase contact line where the colored arrows indicate the location of ridges. (b) A schematic illustration explaining the mechanism of the directional step flow across channels formed by the prism array.

Figure 3-8. Schematic illustrations explaining the relationships of critical contact angles for three directions. Direction 1 means that a liquid droplet flows across the ridge of PNIPAAm surface. Direction 2 is toward the Pt-coated direction. Direction 3 is out of the prism array. Because the critical contact angle could be obtained by $\theta_c = \theta^* + \alpha$, the edge angle is very important to critical contact angle. In the case of direction 3, α is 90° and

Nomenclature

f_i	Retention force to the ith direction
w	Width of a channel
Γ	Surface tension of a liquid
θ_r	Receding contact angle
θ_a	Advancing contact angle
θ^*	Equilibrium contact angle
α	Angle subtended by a ratchet structure forming a solid edge
r_p	Radius of pore
ΔW	Hysteresis in the adhesion energy
ΔP_L	Laplace pressure

Chapter 1. Introduction

Multiscale structures in biological surfaces in nature provide intriguing properties including superhydrophobicity of louts leaf, directional adhesion of gecko feet, antifogging of mosquito eye, directional wettability and structural color of morphobutterfly wings.(*1-6*) These unique functions which are attributed from multiscale architectures have received great attention and have been extensively studied for decades.(*7-18*) Recent advances in material science and miniaturization technology have brought innovative outcomes in biomimetic researches.(*19-22*) In particular, polymeric architectures with the complex and hierarchical forms have been rationally emerged, almost invariably, from multiscale necessities to overcome engineering issues in single scale.(*23-25*) It has been known that, in most cases, microstructures provide enhanced mechanical stability and nano structures give unique functions.(*24, 25*) With the aid of micro- and nanofabrication methods, the miniaturization of conventional fluidic systems for novel analytic systems and the development of polymer electrolyte membrane fuel cell composed with porous electrode with carbon supported Pt particles have been achieved for several decades. (*20, 21, 26-28*) However, a realization of complex, three-dimensional architectures is still challenging with soft materials.

Furthermore, integration of the unique structure in applied system or device is also obstacle to overcome.

Microfluidic system that have advantages of Increased throughput, smaller volumes, easier fabrication and shorter analysis time have received attention for its applications for biological research, healthcare, and food industry. (*20*) Despite increasing demands on miniaturized analytical systems, they still have obstacles for practical applications partly due to their relatively complicated and expensive operation schemes. For example, current microfluidic devices frequently require external tubes and pumps along with an additional integration to the device for the overall miniaturization and portable uses.(*29-31*) Also, the precise manipulation of flows is a remaining issue in the current system. In this aspect, multiscale or asymmetric structures embedded in microfluidic chip without external device can be useful tool to manipulate flow as engineer designed.

Similarly, polymer electrolyte membrane fuel cell (PEMFC) system which is energy conversion device with advantages of low operating temperature and high power density produces water by electrochemical reaction of inserted hydrogen and oxygen gas. PEMFC system involves the continuous production and transport of water in the membrane electrode assembly (MEA) needs to be manipulated for enhanced water transport because if water is not well removed from catalyst layer, it severely inhibits the oxygen transport to catalyst leading to

rapid increase of resistance in the system.(*32*) In addition, Nafion membrane that selectively transport proton ion is main factor to determine performance of fuel cell. Thinner membrane can provide better performance, yet it induces lower mechanical strength and poor processability.(*33*) In this aspect, multiscale approaches with polymeric architectures give methodological breakthrough to enhance performance of polymer electrolyte fuel cell.

To address the remained issues and overcome the limitations, we employed novel and facile methods to achieve multiscale or asymmetric structures via controlled oxygen-inhibition effect of UV-curable materials and guided UV light transmission. The structures were composed with polymers that have their inherent properties as well as easy and low-cost processibility in the systems. (*22, 34*) Especially, we also applied thermally responsive polymer (poly(N-isopropyl-acrylamide)) that switches from hydrophobic to hydrophilic below its Lower Critical Solution Temperature (LCST) of ~32 ℃ into microfluidic system and polymer electrolyte membrane fuel cell system. The polymer gives active component into specific system depending on temperature variation. With the nature-inspired multiscale structures employed proper chemical composition, we could exhibit directional liquid control in microfluidic system and achieve enhanced performance of polymer electrolyte membrane fuel cell. In microfluidic system, we demonstrate *in situ* realization of asymmetric ratchet structures within microchannels by directionally guided light transmission and their directional

flow behavior and thermoresponsive switching of liquid flow direction on a two-face prism array. Futhermore, we improve performance of polymer electrolyte membrane fuel cell by improvement of water transport in PEMFC by selective functionalization of thermally responsive polymer onto carbon-supported Pt and using enhanced proton conductivity with increased reaction area of ultra-thin and free-standing multiscale nafion membrane fabricated by nanoimprint lithography with hierarchical, multiscale structures.

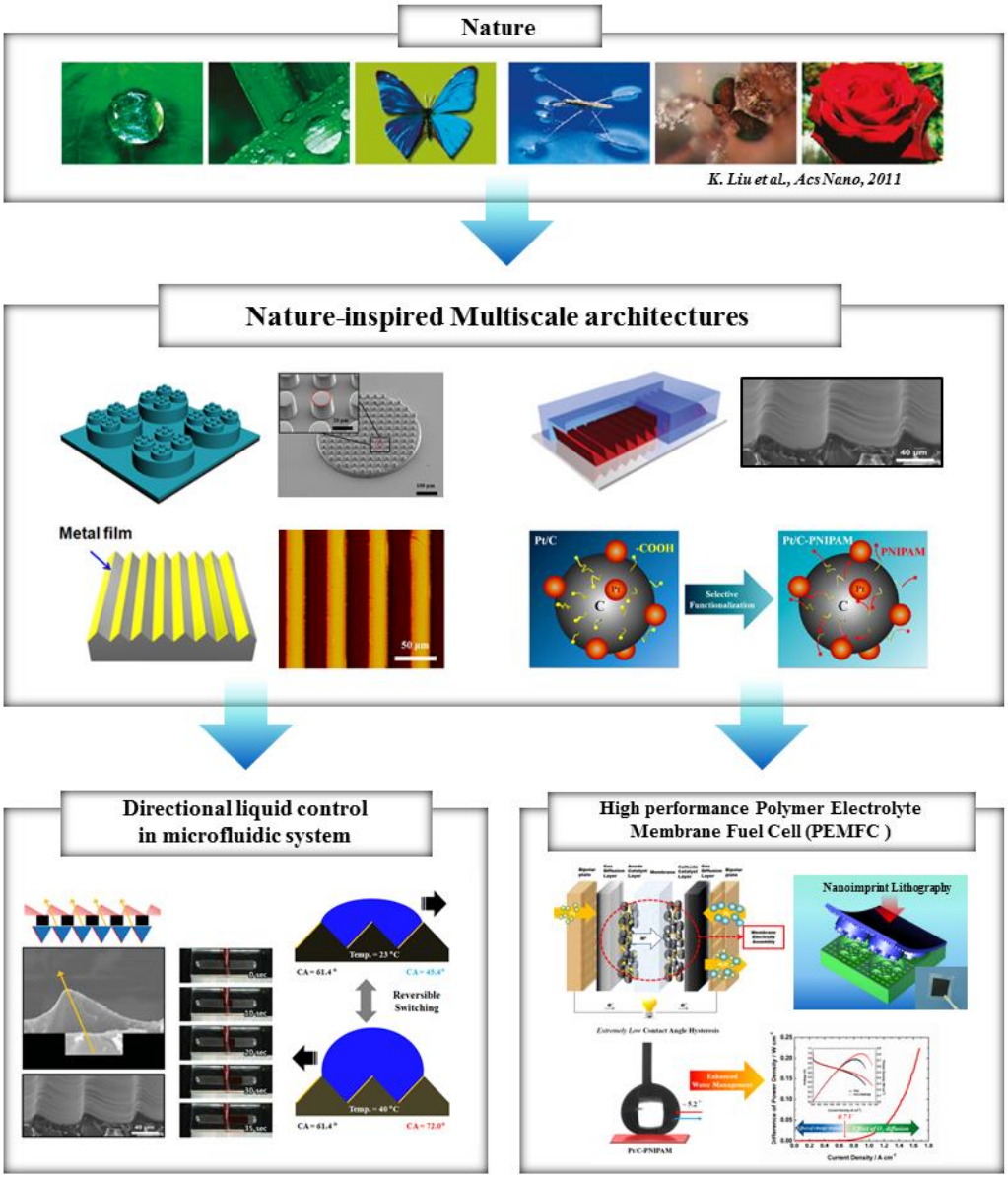

Figure 1-1. Considerable multiscale architecturing processes inspired from nature(*25*) and its applications for directional liquid control in microfluidic system and high performance polymer electrolyte membrane fuel cell (PEMFC)

In ***Chapter 2***, we propose methodological breakthroughs to achieve multiscale structures mimicking biological surfaces in nature. Representatively, multiplex lithography via stacking designed polymeric membrane provides possibility for hierarchical design of pattern dimension at each layer and number of layers. The facile yet versatile strategy for multiscale structures from soft materials allows structural deformations on surface and enables LEGO® -like, monolithic integrations of them by quantitatively controlling the oxygen-inhibition effect of UV-curable materials. Micro ebb tides of partially cured resin were observed and utilized to form dual phase brick with viscoelastic coating that was promoted to be nanopatterns and connections under multiple UV exposures. Furthermore, to realize asymmetric ratchet structure in morphobutterfly wings or water strider legs, we developed a simple but powerful strategy to directly program asymmetric structures within a microchannel by combination of photopolymerization within a microchannel and the guided light transmission through an optically asymmetric Lucius prism array.

In ***Chapter 3***, we present the asymmetric ratchet structures, created at the bottoms of microchannels, show the unidirectional liquid flows as well as controlling the fluid speed in a predefined region. Then, we demonstrated two examples of asymmetric structures created or programmed in specific regions within microchannels to control the fluid speed in predefined regions and to be

used as on-chip timers in split microchannels. In addition, we present a simple approach to reversibly switch the direction of liquid flow on physically symmetric and chemically asymmetric prism structures by exploiting the reversibility of wetting properties on a thermo-responsive polymer, poly(N-isopropyl-acrylamide) surface is demonstrated. Such an asymmetric prism array creates a flow path in the direction of the lower critical contact angle. This allows a unidirectional "step flow" across the ridges of prism channels, which can be made reversible with suitable temperature change.

In ***Chapter 4***, we demonstrate enhancing performance in polymer electrolyte membrane fuel cell (PEMFC) via multiscale approaches. To improve mass transport in cathode electrode, carbon-supported Pt (Pt/C) catalyst was selectively functionalized by a thermally responsive poly(N-isopropylacrylamide) (PNIPAM) to improve water transport in the cathode of proton exchange membrane fuel cell. Amine-terminated PNIPAM selectively reacted with the functional group of –COOH on carbon surfaces of Pt/C via the amide reaction by 1-ethyl-3-(3-dimethylaminopropyl)carbodiimide (EDC) as a catalyst. Pt surfaces of Pt/C were intact throughout the carbon surface functionalization, and the carbon surface property could be thermally changed. The PNIPAM-functionalized Pt/C was well dispersed due to its hydrophilic surface property at room temperature during the catalyst ink preparation. In sharp contrast, when PEMFC

was operated at 70 ℃, PNIPAM-coated carbon surface of Pt/C became hydrophobic, which resulted in a decrease in water flooding in the cathode electrode. Due to the switched wetting property of the carbon surface, PEMFC with PNIPAM-functionalized Pt/C catalyst in the cathode showed high performance in the high current density region. To explain the enhanced water transport, we proposed a simple index as the ratio of systematic pressure (driving force) and retention force. Furthermore, to demonstrate the effectiveness of multiscale engineering, complex and multiscale architectures with an aid of multiplex lithography that integrates rational advantages in both microscale and nanoscale, was embedded into fuel cell devices to fully probe advantages of each scale pattern, resulting in outstanding device performance by increasing both proton conductivity and surface area for electrocatalysis.

Chapter 2. Multiscale Design and Fabrication of Polymeric Architectures

2-1. Multiscale architecturing by quantitatively controlled oxygen-inhibition effect of UV-curable materials

2-1-1. Introduction

Soft lithography, a rapid prototyping of structures geared to both microscale and nanoscale, is a collection of versatile techniques, displaying impressive patterns and incorporating them into advanced applications with an aid of flexible, elastomeric stamps.(*35*) Such a flexibility that is an inherent property of soft material has significantly improved technologies in the fields of artificial sensors(*36*), wearable electronics(*37, 38*), optical and energy devices(*39, 40*). Also, it has even accelerated capabilities for real-actuating, soft robotics(*41*) by applying additional stimulus to original figures. This appealing characteristic enables a certain degree of elastic/plastic deformation when external forces are applied, thereby providing potentials for achieving a complex, hierarchical engineering(*42*). For example, rational mechanical deformations including

stretching(*43*), bending(*42*) and bulging(*36*) of elastomers and chemical modifications on given surfaces(*44*) have been demonstrated widely as strategies to get complex structures by taking advantages of elasticity in soft materials and provoking material instability.

The complex, hierarchical microarchitectures have been rationally emerged(*45*), almost invariably, from multiscale necessities to overcome engineering issues in single scale(*23, 24*), while a realization of complex, three-dimensional architectures is still challenging with soft materials. This is mainly due to the fact that soft lithography basically employs sufficient thermal or ultraviolet (UV) treatment to solidify the raw materials for high pattern fidelity. To achieve hierarchical deformations with fully solidified patterns, thermo-mechanical deformation that is a thermal reflow in confined guidance, is useful for processing secondary/tertiary imprint onto pre-defined thermoplastic structures around the glass transition temperature(*46*, *47*) via imprint lithography named by Chou et. al.(*48*). However, those types of thermal deformations give rise to several practical problems owing to stress instability from a difference in thermal expansion of materials or layers, which potentially restricts a facile embedding of hierarchical structures to engineering applications(*49*). In the case of UV-curable materials that guarantee simple yet rapid replication within minutes in both microscale and nanoscale are typically manipulated to be patterns under a concrete cross-linking within polymer chains, restricting reliable and sustainable

secondary deformations onto predefined structures except the cases of restorations from elasticity and mechanical failures after fracture point. Moreover, successful realization of multiscale, hierarchical architectures into engineering devices is obviously difficult due to the rarity of those complex patterns and lack of suitable embedding processes in engineering fields. To address those challenges, we demonstrate a multiplex lithography that is facile strategy for a multiple, stepwise treatment of UV-curable resin under a quantitatively controlled oxygen-inhibition effect to form multiscale, hierarchical architectures via a replica molding (REM)(*23, 50*). A LEGO® -like deformation and multiplex stacking of dual phase bricks are described in here mimicking lotus leaf or petal.

2-1-2. Experimental

Preparation of PDMS patterned array.

The hole patterned silicon masters were fabricated by photolithography and reactive ion etching. The masters were treated with a fluorinated-SAM solution ((tridecafluoro-1,1,2,2-tetrahydrooctyl)-trichlorosilane:FOTCS, Gelest Corp.) diluted to 0.03 M in anhydrous heptane in an Ar chamber. After the surface treatment the masters were annealed at 120℃ for 20 min. After the preparation of the master, a mixture of base and curing agent (10:1 w/w) of Sylgard 184 PDMS elastomer (Dupont) was poured onto the patterned masters and cured at 70 ℃ for 2 h. The cured PDMS molds were peeled off from the master and cut prior to use.

Fabrication of UV cured dual phase polymeric membrane.

A small amount of hydrophilic resin (PUA311, Minuta Tech) was drop-dispensed onto a patterned PDMS mold, and a flat PDMS upper mould was uniformly placed onto patterned PDMS mold. Then, the sandwich assembly was exposed to UV light (< 3 min, λ = 250~400 nm, Fusion Cure System, Minuta Tech) under an applied pressure (25 g cm^{-2} ~ 1 kg cm^{-2}) after forming conformal contact. After removal of the upper and lower PDMS molds, a flexible, free-

standing membrane with dual phase polymeric membrane via micro ebb-tide phenomena was obtained.

Multi-stacked, multi-dimensional pattern array with simultaneous imprinting & bonding process.

A prepared dual phase polymeric membrane was uniformly placed onto nanopatterned PUA311 mold contacting with more cured face (α phase) of the membrane and nanopatterned PDMS mold was placed onto the less cured face (α′ phase) of the membrane. Then, the sandwich assembly was exposed to UV light (> 3 min, λ = 250~400 nm) with hydraulic pressure (6~8 kg cm^{-2}) in a vacuum chamber (5×10^{-2} Torr) after forming conformal contact. After removal of the PDMS molds, multiscale two-level PUA311 hole pattern array via simultaneous bonding and imprinting process was obtained. The same process was conducted with different micro-sized membrane to obtain tri-level PUA311 hole patterned master. After the preparation of the master, a mixture of base and curing agent (10:1 w/w) of Sylgard 184 PDMS elastomer was poured onto the patterned masters and cured at 70 ℃ for 2 h. The cured PDMS molds were peeled off from the master and cut prior to use.

2-1-3. Results and Discussion

The key features from multiplex lithography are briefly illustrated in **Figure 2-1**, where multiscale perspective reveals complex, three-dimensional architectures that contain respectively different nanopatterns onto each level of hierarchical surface (**Figure 2-1b**). This unique structural hierarchy is oriented from scavenging effect of infiltrated oxygen near a highly permeable polydimethyl siloxane (PDMS) blanket, remaining a thin layer of permitted oxygen owing to inhibition of radical-induced polymerizations(*51*) (**Figure 2-1c**). A monitoring with relative peak height of Fourier-transform infrared (FT-IR) spectra shows a gradual, multiplex curing of polyurethane acrylate (PUA) under time-dependent UV-curing reaction (**Figure 2-1d**) (*52*), where PUA resins with low curing contrast (i.e., ranges 30~55%) remain a lot of cross-linkable bonds on a soft, viscoelastic surface that is capable of sequential curing with LEGO® -like deformation in our experiments. We hypothesize that two types of paths are possible from permeability differences in boundary conditions; i) slow curing under a highly permeable blanket (PDMS, dashed red line) and ii) fast curing under a blanket with low permeability (PUA, dashed black line), where close correspondence in slope is represented with same color of arrows and dashed lines (**Figure 2-1e**). The detailed explanation for hypothesis is further followed below with multiplex curing steps, consisting of a preparation of dual phase bricks (α

and α′), a confined LEGO®-like deformation (β’) and a monolithic bonding of each brick (β and γ). The first step for multiplex lithography is a generation of a dual phase membrane by partially curing the PUA resin between permeable PDMS layers that are constructed with a sandwich-like assembly (**Figure 2-2a**). Here, overlapped OIL within the confined, thin PUA was readily achieved when simple squeezing was processed, due to hydrophobicity differences near interfaces (i.e., contact angle of PUA and PDMS is approximately 88° and 104°, respectively). After a first, short UV treatment, the confined PUA layer was divided into two parts via disassembly, generating a partially cured PUA brick with low curing contrast (red dashed box). Then, the brick experiences a spontaneous dewetting that provokes a lot of individual micro ebb tides of viscoelastic resin on an array of exposed PDMS pillars (purple arrows). Note that the PUA showed low affinity against to the hydrophobic PDMS surface, thus the micro ebb tides (movement of PUA droplet) were slowly headed for PUA surface (**Figure 2-2b**), resulting in a dramatic drop of curing contrast (α → α′) because the droplet was initially placed at overlapped OIL regions so that permitted oxygen could prohibit the UV reaction seriously. The microscopic images in **Figure 2-2b** are monitoring scenes for the micro ebb tides that act as automatic viscoelastic coating onto a neighboring PUA brick. As an initial step, a long wave occurs rapidly by surface tension of uncured PUA resin (green arrows). Then, the individual viscoelastic droplet started to move induced by affinity mismatching

(purple arrows). This type of dewetting lasted for several minutes (> 1 min) constantly and slowly, where similar dewetting is also detectable on the disintegrated flat PDMS layer. After dewetting, self-supporting polymer brick with viscoelastic coating on top surface was obtained by removing the underlying PDMS mold from the assembly. Notably, independent to pattern shape and dimension, dual phase membrane bricks can be achieved via presented phenomena. In addition, the brick is sufficiently robust to be handled with tweezers without cracking or tearing with an aid of connected frameworks of the PUA brick that has relatively high elastic modulus (~ 320 MPa) (**Figure 2-2c**). The **Figure 2-2c** is a representative digital image of the dual phase brick with 150-μm apertures over a large area of up to 2 inches, which used in a LEGO®-like multiplex process.

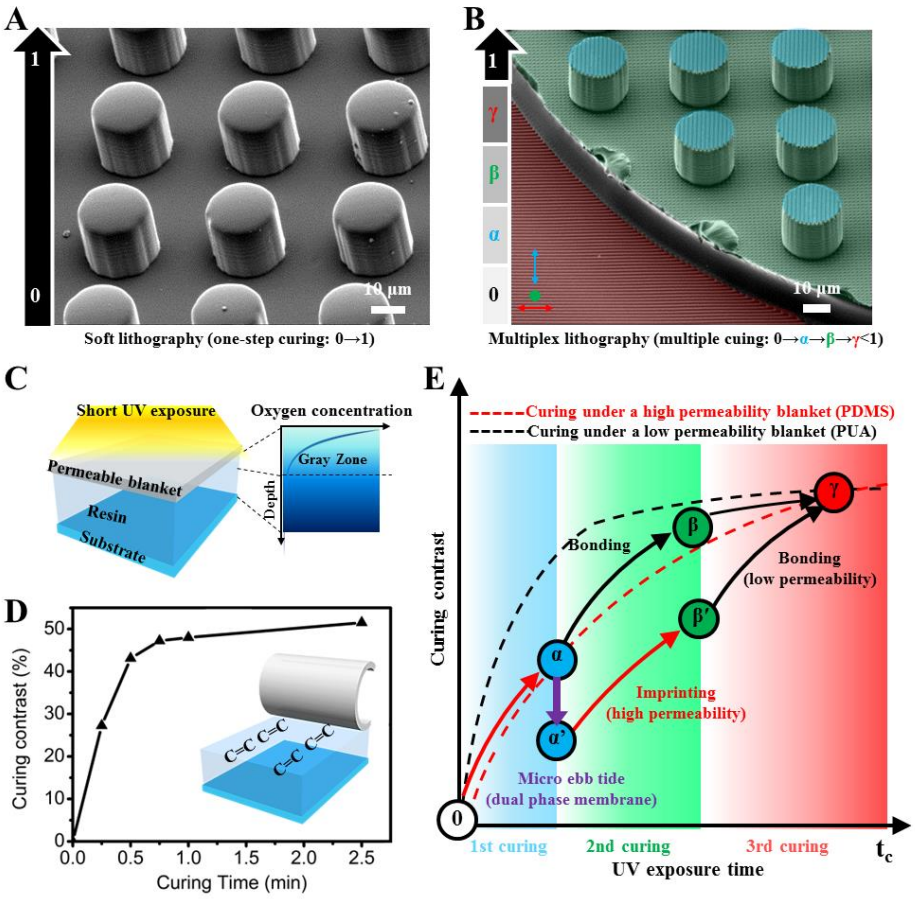

Figure 2-1. Multiscale perspective and hypothesis for a multiplex lithography. (a) Single scale structures from a soft lithography. (b) Multiscale perspective of a complex, hierarchical architecture from a multiplex lithography. The architecture has individual nanopatterns (dots and lines) on each flat surface. (c) Illustration of a ‘gray zone’ with permitted oxygen from a permeable PDMS blanket. (d) Calculated curing contrast after time-dependent, short UV exposure. (e) A hypothesis for multiple curing with UV to form complex, hierarchical architectures from simple molding processes.

To elucidate the function of the dual phase membrane, curing contrasts of viscoelastic layer on a dual phase brick were discussed by using FI-IR and focused ion-beam milling studies. When a surface with curing contrast of α (55%) is attached onto the pattern with nano holes, they remain clearly unfilled nanoholes under a bonding interface (surface bonding), while even microscale holes were filled (structural interconnection) under a deformed viscoelastic layer of α′ (45%) which gives possibility to carve patterns onto the brick directly. For the experiment, the both underlying holey patterns were treated as 60% for good pattern fidelities in hierarchical structures after replications. This monolithic integration concept was further verified by stacking various bricks and replicating with materials for successful multilevel architectures of up to four levels. The schematic illustration of **Figure 2-3a** depicts a LEGO® -like multiplex process that employs aforementioned two independent curing paths relating to sequential imprinting and bonding. Basically, the brick has two different curing contrasts at both sides (α and α′); monolithic integration is processed with the bottom of brick (~ 55%) by placing the brick onto a pre-patterned PUA with curing contrast of β (~ 60%). The scanning electron microscopic (SEM) image in **Figure 2-3b** shows 800-nm-patterned PUA holes (depth: 800 nm) as an underlying substrate for a monolithic integration. Then, both dual phase membrane with 20-μm-holes (thickness is 20 μm, **Figure 2-3c**) and permeable mold with nanopatterns (800-nm-dots) were vertically placed and pressed to deform the viscoelastic coating for

confined nanostructures (imprinting), while bottom layer bonded to underlying patterns (bonding) during second UV exposure (**Figure 2-3d**). According to the hypothesis, the PUA brick has low permeability; the underlying bonding follows fast curing regime, however, the same, second exposure leads to stepwise increases in curing contrast of up to 60% that is sufficient values for next bonding step during third exposure. By repeating the multiplex stacking (iv, v, vi), a third layer was integrated (**Figure 2-3e**), where 800-nm-holes are clearly observed on every projected surface. As a final step, we performed a replica molding with various pre-polymers to robustly form a tri-level hierarchical architecture from a fully cured assembly ($\gg$ 60 %, vii) as shown in the **Figure 2-3f**. It should be noted that the multiplex curing and stacking is rationally processed by controlling the curing contrast with permeability, together with the micro ebb tides for effective reduction of curing contrast on top surface of brick, which would be a unique strategy as a guide for multiscale, hierarchical engineering with polymers via facile molding approaches.

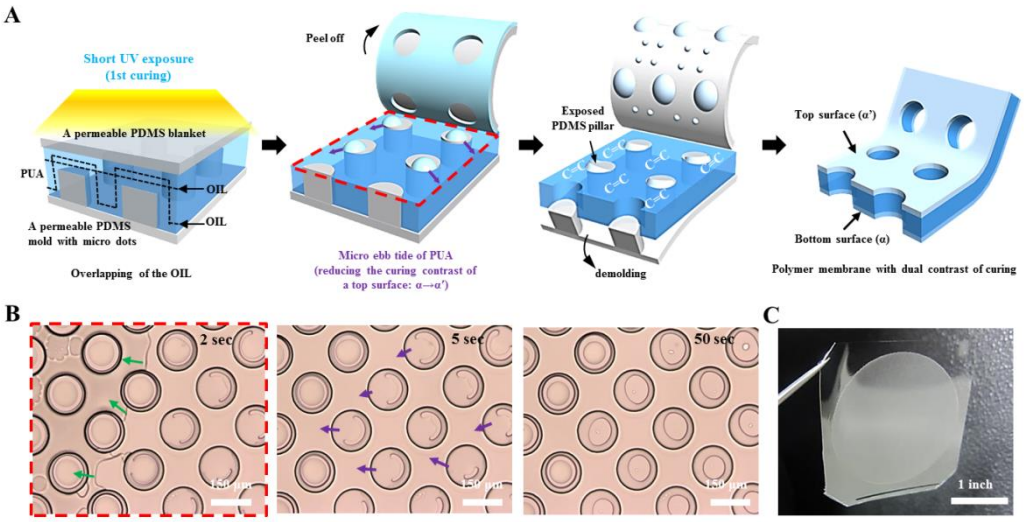

Figure 2-2. Micro ebb tides of partially cured resin for a generation of dual phase membrane. (a) Schematic illustration for overlapping of OIL and resulted micro ebb tide after 1st UV exposure. The micro ebb tides reduce a curing contrast on top surface of brick from α to α′ rationally. (b) Microscopic images for real-time monitoring of micro ebb tides. Note that low affinity of viscoelastic PUA resin onto PDMS pillars yields spontaneous coating of partially cured resin on the top surface of brick. (c) Digital image of the obtained dual phase brick as a unit part for LEGO® -like deformations. (Cited from doctorate thesis in Seoul National University, Hyesung Cho, 2012, Multiscale, multilevel architectures and polymeric stencils by partial curing and dewetting method)

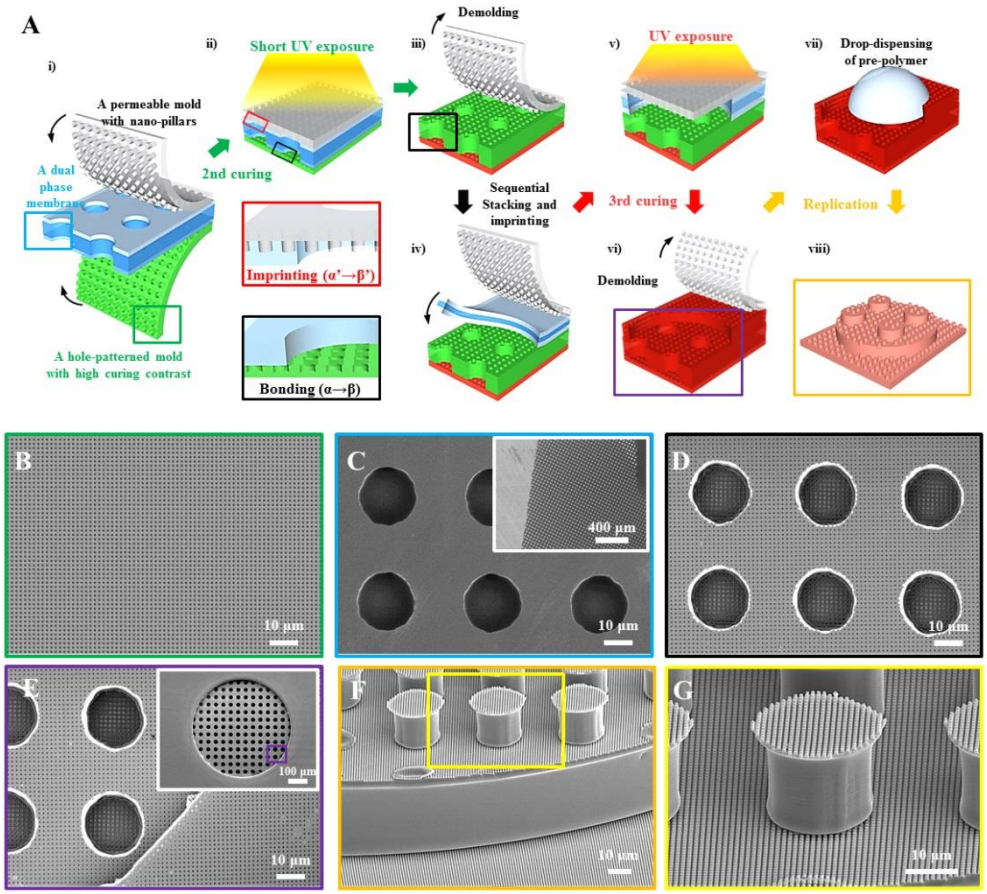

Figure 2-3. LEGO® -like, multiplex lithography procedures. (a) Schematic illustration for the multiplex lithography process by vertical stacking and imprinting each dual phase brick. Both imprinting and bonding is achieved with the top and bottom surface of brick to form complex, hierarchical architectures. (b to g) SEM images for the corresponding structures.

2-1-4. Summary

We developed facile yet versatile strategy for multiscale structures from soft materials that allows structural deformations on surface and enables LEGO® -like, monolithic integrations of them by quantitatively controlling the oxygen-inhibition effect of UV-curable materials. Micro ebb tides of partially cured resin were observed and utilized to form dual phase brick with viscoelastic coating that was promoted to be nanopatterns and connections under multiple UV exposures. The realization of complex, multiscale architectures is of significant interest and incorporation of those structures into engineering application provides methodological breakthroughs in practical issues with an aid of multiscale approach that integrates rational advantages in both microscale and nanoscale.

2-2. Multiscale, asymmetric ratchet structures within microchannels via guided UV light transmission

2-2-1. Introduction

In nature, biological creatures including insect, plant and animal own specific multiscale, asymmetric micro/nano structures on their surfaces to adapt to surrounding environments provided. For example, gecko lizard possess numerous tilted micro/nano hierarchical hairs(setae) on their foot to climb up any barrier even vertically soared wall to adapt rugged geometric environment (*50*). Asymmetric micro/nano structures also exist on the surface of morpho butterfly's wings. The asymmetrically arranged ratchet-like structures allow water droplet falling on the wing surface to roll down from body to the outside preventing congesting water on the body (*24, 25, 53*). Moreover, some kinds of plant's leaf surface including rice leaf with aligned fabrics let water fluid flow to the aligned direction cumulating water efficiently (*24, 25, 53*). Definitely, the roles of the asymmetric micro/nano structure are diverse with specific functions.

Inspired from the inherently unique properties of the asymmetric structures in nature, extensive efforts applying the properties to technological research fields including dry adhesive, wetting, electronics and tissue engineering (*53*) with directional property have been accomplished in past decades.

Corresponding with the needs for directional property of micro/nano structures, diverse fabrication strategies for forming anisotropic structures on target substrate have been tried to achieve the specific aim. Generally anisotropy (or asymmetry) imply directional dependant properties with different axes as opposed to isotropy (or symmetry) exhibiting equivalent properties in all directions. In the aspect of the definition, line (i.e. Aligned string), bended hair, tilted textured surface, helical structure, triangular structure, wavy shape holding anisotropy in geometry can be categorized anisotropic structure. The geometrically anisotropic structures with scaling down to micro/nano size induce directional guidant functions to water droplet, electrons and cells on the substrate and also assign directional adhesion to tiny hairy structures. To get the target structures corresponding to specific purpose of utilizing directional function, proper fabrication strategy should be set up considering suitable and processable material, substrate, catalyst and possibility to get target shape and size-limitation.

Herein, we present a direct and facile method to realize programmed multiscale and asymmetric structures within microchannels by combining photo-polymerization with the directional transmission through an optically asymmetric film named as the Lucius prism array,(*54, 55*) which is a prism array with one facet sides coated with metal films.

2-2-2. Experimental

Fabrication of Lucius prism array

In this paper, we used the *Lucius* prism array with 50 μm in period and 45˚ in prism angle. After the preparation of the polymeric prism array by the replica molding, we deposited ~100 nm thick Cr metal films on one faces of the prism array using an oblique metal evaporation. We used a E-gun evaporator (V-system) for the metal deposition and placed the polymer prism array on an inclined holder with an angle 60˚. The detail procedure of the fabrication can be found elsewhere.

Fabrication of asymmetric ratchet structure in microfluidic system

Microfluidic channel (3 mm in width, 200 μm in height) composed of polydimethylsiloxane (PDMS; Sylgard 184, Dow Corning) was prepared with the mixing ratio of 10:1 (prepolymer: curing agent) and curing temperature of 60℃ for 2h. Then, the PDMS channel punched with two holes for inlet and outlet of fluid was bonded onto a glass sheet (150 μm of thickness). For the fabrication of asymmetric ratchet structure in microfluidic channel directly, ultraviolet (UV)-curable polyurethaneacyrlate (PUA) prepolymer was filled into the channel and photomask of line shape with a width of 40 μm and a space of 40 μm and the Lucius prism array was arranged onto the backside of glass substrate layer by

layer. Then, vertical UV exposure (400 mJ cm^{-2}, 365 nm in wavelength) to the Lucius prism array for 10 sec induced crosslinking of prepolymer in microchannel resulting in asymmeric ratchet structure. The unreacted prepolymer was rinsed with DI water several times and fabricated structures was dried in a dry oven for more than 4 h.

2-2-3. Results and Discussion

A schematic illustration on the direct realization of asymmetric structures using a Lucius prism array is shown in **Figure 2-4**. At first, a microfluidic channel (3 mm in width and 200 μm in height) made of poly(dimethyl siloxane) (PDMS) was prepared. After making a microchannel pattern with the conventional photolithography, we cast a mixture of PDMS precursors (Sylgard 184, Dow Corning) onto the photoresist pattern. PDMS curing at 60 ℃ was then performed at a mixing ratio of 10:1 (prepolymer: curing agent). After the cure, the PDMS channel was detached from the photoresist pattern. The PDMS channel was then glued onto a glass plate (150 μm in thickness) with two holes for liquid injection. To create polymeric structures within the microchannel, we filled the channel with low-viscosity UV-curable polyurethaneacyrlate (PUA) prepolymers.(*56*) In order to guide UV light with a defined direction, an optically asymmetric Lucius prism array was placed between the light source and a photomask, as shown in **Figure 2-4a**. The Lucius prism array was prepared by the micro-molding with UV curable polymers (PUA, 311RM)(*57, 58*), followed by the oblique metal deposition to coat metal films only on one sides of the prism array. The detailed procedure to prepare the Lucius prism arrays can be found elsewhere.(*54*, *55*) Because the left faces of the prism array are blocked by metal films, the straight incident light is bent toward the left direction, as shown in **Figure 2-4b**. After

slanted UV exposure (with 365 nm in wavelength and an intensity of 400 mJ cm^{-2}) of the PUA prepolymers trapped within the microchannel, the unreacted PUA prepolymers were removed by rinsing with DI water several times. The asymmetric ratchets, created within the microchannel, were then dried in a dry oven for more than 4 hrs.

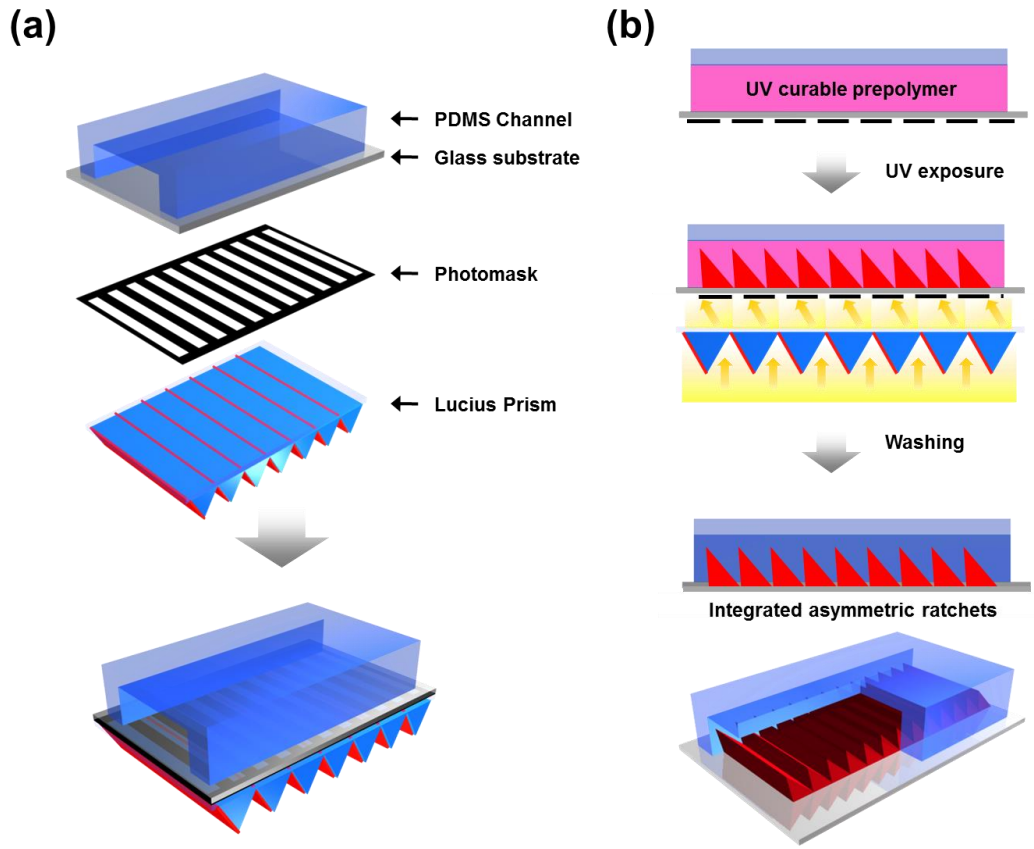

Figure 2-4. (a) An overall scheme for the integration of asymmetric structures within a microchannel, which is composed of a PDMS channel on a glass substrate, a photomask and the Lucius prism array. (b) A schematic illustration of the realization of asymmetric structures in a microfluidic channel by the guided transmission through the Lucius prism array.

Figure 2-5 shows the scanning electron microscopic (SEM) images of a symmetric structure generated within a microchannel without using the Lucius prism array (**Figure 2-5a**) as well as an asymmetric structure created with the Lucius prism array (**Figure 2-5b**). The designed photomask lines have a width of 40 μm with a spacing of 40 μm. **Figure 2-5b** demonstrates the photopolymerized asymmetric structure created from the same mask pattern when the Lucius prism array was placed just below the mask. It is noted that the tilt angle is 21 degree, which is in good agreement with the Snell's law, as we discussed in the previous paper.(*55*) We further notice that the line mask pattern yielded the symmetric triangular polymer structure even without the Lucius prism array after curing, presumably due to non-uniformity of UV intensity within the microchannel filled with PUA prepolymers. The simulation on the light path in the presence of the Lucius prim array is given in **Figure 2-6**.

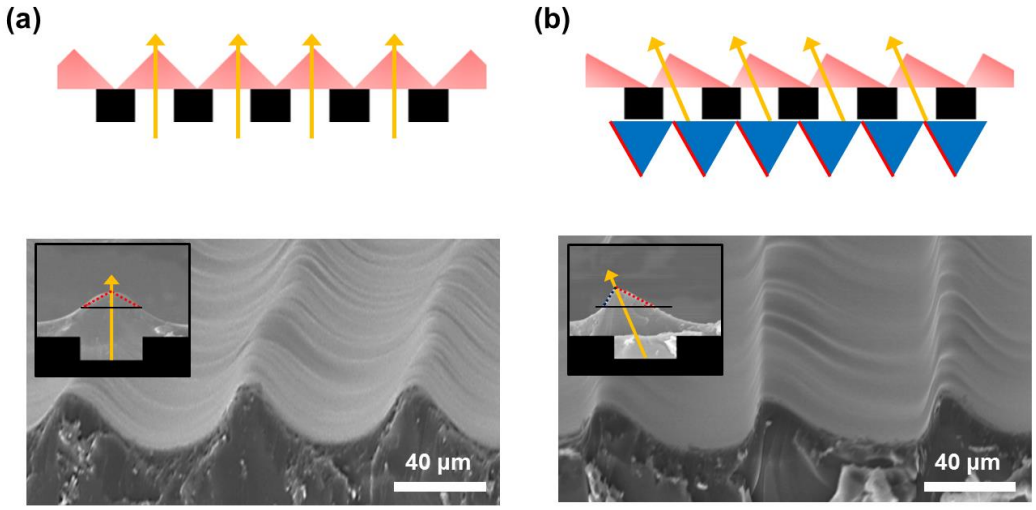

Figure 2-5. SEM images of polymeric structures realized within microchannels after UV illumination. (a) Symmetric microstructures fabricated without Lucius prism array. (b) Asymmetric microstructures fabricated with Lucius prism array.

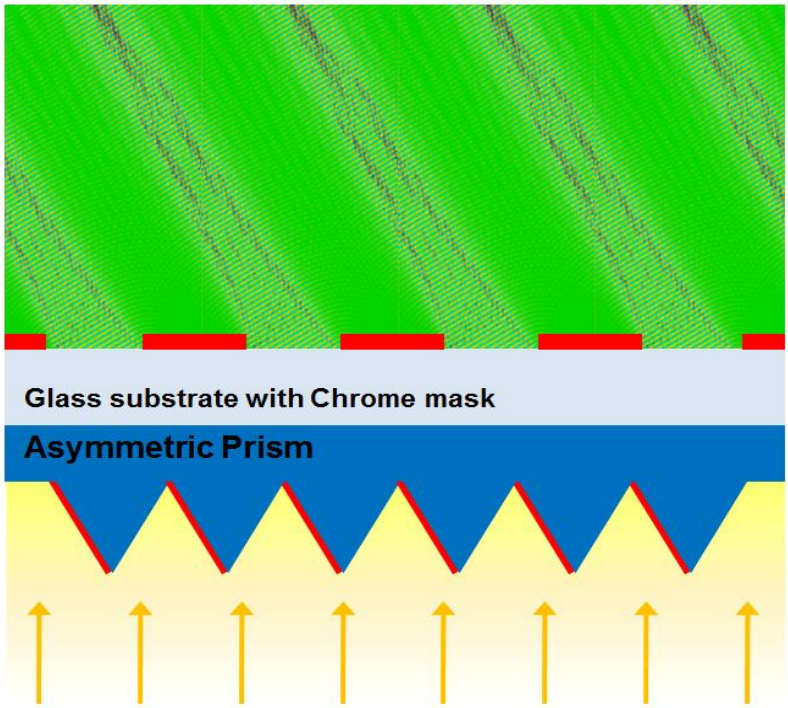

Figure 2-6. A light path geometry and light-intensity distribution calculated from the EM-Explorer program. The UV-light within a microchannel was refracted by the Lucius prism array because the left sides of the prism array are blocked by metal films (PUA refractive index = 1.5, UV light intensity = 400 mJ cm^{-2}, 365 nm in wavelength).

2-2-4. Summary

We present a simple but powerful strategy to directly realize or program asymmetric structures within a microchannel by a combination of photopolymerization within a microchannel and the guided light transmission through an optically asymmetric Lucius prism array. We took advantage of the selective light refraction into one direction through the optical Lucius prism array to crosslink liquid prepolymers within a channel, yielding asymmetric ratchet structures.

Chapter 3. Multiscale Architectures for Wettability Control in Microfluidic System

---

Published in Advanced Materials, 2014, 26, 2665 (*59*)

Published in Soft Matter, 2013, 9, 4145 (*54*)

3-1. In Situ Realization of Asymmetric Ratchet Structures within Microchannels by Directionally Guided Light Transmission and Their Directional Flow Behavior

3-1-1. Introduction

Recently, asymmetric structures inspired from the Mother Nature have extensively received attention because of their unique physical properties such as directional wetting, directional adhesion, and directional transmission for their applications in microfluidic devices, dry adhesives, and three-dimensional displays. (*50, 54, 55, 60-70*) More specifically, directional wetting has been reviewed in detail several times for their potential use in microfluidics and biomedical devices.(*60-62*) For example, Kim et al.(*63*) demonstrated that “stooped” nanohairs could control the fluid velocity within microchannels and Malvadkar et al.(*64*) developed slanted nanorods for drag reduction on nanofilms.

These achievements have been expected to control liquid flow in microfluidic assays, in which sequential delivery of multiple reagents in detection regions and temporally controlled reagent transport are strongly needed.(*71-73*) Although many researchers have developed different versions of fabrication methods to realize the asymmetric structure, we are still in need for improved techniques to integrate the asymmetric structures within microchannels in simple and economic ways because the integration process of patterned structures within microfluidic channels is typically complicated. For example, bonding and sealing processes of microchannels on the asymmetric patterns with precise alignment should be required. Here, we present a direct and facile method to realize programmed asymmetric structures within microchannels by combining photo-polymerization with the directional transmission through an optically asymmetric film named as the Lucius prism array,(*54, 55*) which is a prism array with one facet sides coated with metal films. The Lucius prism array can refract incident rays with an angle through one facet sides of the prism array while light from the other sides for the prism is reflected off the coated metal films. By selective and directional UV exposure through the prism array onto photo-curable prepolymers filled within a microchannel, one can obtain polymeric asymmetric structures within the channel after removing uncured prepolymers. The novelty of the proposed direct integration with the Lucius prism array is the ability to control angled directions in judiciously designed prism areas by one-step photo-polymerization.

Furthermore, we demonstrate two examples of the direct integration of asymmetric structures within microfluidic channels to control the fluid speed on asymmetric ratchet surfaces as well as the rate-dependent channel filling showing different dwell times in a split channel.

3-1-2. Experimental

Physical analysis

SEM images were taken using FESEM (Hitachi S-48000, Japan). Liquid flow movie cuts were obtained by a digital video camera (SONY DSC-T30, Japan).

Fabrication of asymmetric ratchet structure with variation of orientation in a designated area within a channel

Microfluidic channel (3 mm in width, 200 μm in height) composed of polydimethylsiloxane (PDMS; Sylgard 184, Dow Corning) was prepared with the mixing ratio of 10:1 (prepolymer: curing agent) and curing temperature of 60℃ for 2h. Then, the PDMS channel punched with two holes for inlet and outlet of fluid was bonded onto a glass sheet (150 μm of thickness). For the fabrication of asymmetric ratchet structure in microfluidic channel directly, ultraviolet (UV)-curable polyurethaneacyrlate (PUA) prepolymer was filled into the channel and photomask of line shape with a width of 40 μm and a space of 40 μm and the Lucius prism array which was designed to tilt incident light to the right direction in the areas A and C while bending light path to the left direction in the area B was arranged onto the backside of glass substrate layer by layer. Then, vertical UV exposure (400 mJ cm^{-2}, 365 nm in wavelength) to the Lucius prism array for 10

sec induced crosslinking of prepolymer in microchannel resulting in asymmeric ratchet structure. The unreacted prepolymer was rinsed with DI water several times and fabricated structures was dried in a dry oven for more than 4 h.

Demonstration of liquid flow on asymmetric structures in microfluidic channel

The prepared microfluidic channel was punched in an inlet hole at the center of the channel and dispensed water, colored in red, by gravity to demonstrate the unidirectional liquid flow on the asymmetric ratchet structure created within a microchannel.

3-1-3. Results and Discussion

We made an inlet hole at the center of the channel and dispensed water, colored in red, by gravity to demonstrate the unidirectional liquid flow on the asymmetric ratchet structure created within a microchannel,. When the water is in contact with the symmetric structure within the microchannel, water flows on both directions, as shown in **Figure 3-1a**. On the contrary, when the colored water is forced to touch the asymmetric ratchet structure, water selectively flows toward the right direction, as shown in **Figure 3-1b**. The average speed of the liquid flow was ~ 14 μm /sec and the flow direction selected on the ratchet structure is toward the face with a lower base angle, as shown in **Figure 3-1c**.

To elucidate the different behavior of liquid flow on the asymmetric ratchet surface, we simply set the asymmetric structural model with two base angles of θ_1 (~ 27˚) and θ_2 (~ 59˚), as shown in **Figure 3-1c**. The retention force at a contact line prevents liquid from moving forward, which is expressed below:(*74*)

$$f_i = w\gamma\ (cos\theta_{ri} - cos\theta_{ai})$$

, where f_i is the retention force that resists the incipient motion of liquid acting on the i^{th} direction, w is the width of a microchannel related to the length of contact line, γ is the surface tension of a liquid (i.e., water in the current case), θ_{ri} is the receding contact angle component in the i^{th} direction while θ_{ai} is the advancing contact angle component in the i^{th} direction. In our system, the change of liquid

quantity in the reservoir is negligible despite the liquid flow through the microchannel. Hence, we can assume the receding contact angle as zero. Then, the retention force can be modified as the following:

$$f_i \sim w\gamma\ (1 - cos\theta_{ai})$$

In addition, on the face of ratchet-like structure, the advancing contact angle of the contact line is further increased by θ_i with respect to the advancing contact angle on a flat surface (θ_{a0} : ~ 83.1˚).

$$f_i \sim w\gamma\ (1 - cos(\theta_{a0} + \theta_i))$$

Since we apply a constant external force f_{ext} (= P_{ext} × w × h, P_{ext} and h is the external pressure and the channel height, respectively) on the liquid, the net force f*net* is just the difference between the external force and the retention force (f_{net} = $f_{ext} - f_i$). Then, the retention force ratio (K) with asymmetric ratchet-like structure is described as:

$$\mathrm{K} = \frac{(f_{ext} - f_2)}{(f_{ext} - f_1)} = \frac{[1 - (1 - \frac{\cos(\theta_{a0} + \theta_2)(\gamma/h)}{P_{ext}})]}{[1 - (1 - \frac{\cos(\theta_{a0} + \theta_1)\,(\gamma/h)}{P_{ext}}]}$$

When we set the external pressure and the surface tension to 0.7 kN/m^2 (the gravity of water of 7 cm in height) and 0.0717 N/m^2(*75*, *76*) respectively, the K ratio of 0.27 was obtained for the asymmetric structure created in **Figure 3-1b**. This implies that the net force in the direction 1 (flow right) is bigger than the force in the direction 2 (flow left), indicating a smaller resistance with a smaller

base angle when liquid flow starts. We also note that the ratio K is independent of the channel width as shown in **Figure 3-2**. Also, the retension force could be negligible in comparison with the external pressure when the surface tension of liquid is quite low (i.e., 0.0217 N/m^2 for isopropyl alcohol (IPA), as demonstrated in **Figure 3-3**.(*75, 76*) From this observation, it is interesting that it is only the structural asymmetry that could differentiate the flow velocity with the difference in resistance. We also noted that the direction of liquid flow is determined by the crtical contact angle, as discussed in the previous study.(*54, 77*) The critical contact angle θ_c can be written as follows:

$$\theta_c = \theta^* + \alpha$$

where θ^* is the equilibrium contact angle on a planar surface and α is the angle subtended by a ratchet structure forming a solid edge, which is referred to as the base angle. In the present case, θ^* is the same as the bi-directions because the surface-forming material is the same all over the surface. In the asymmetric ratchet system, the critical contact angles of two faces are different from each other because of their different edge angles.(*74, 77-79*) As a result, the critical contact angle is higher on one side when compared with the other and the liquid front is forced to move in the direction of a lower critical contact angle.

This strategy of realizing asymmetric structures within a channel with a Lucius prism array could easily be extended to control the speed of liquid flow with a predesigned optical Lucius film. **Figure 3-4** demonstrates an one-step

procedure to create a ratchet structure with different orientations with a predesigned Lucius prism array. We could easily control or program the direction of ratchet orientation in a designated area within a channel with the change in the faces coated by metal films to alter the light. In the present study, we prepared a Lucius prism array to tilt incident light to the right direction in the areas A and C while bending light path to the left direction in the area B. We then exposed UV light after filling liquid prepolymers within the channel followed by the removal of unreacted prepolymers. To demonstrate the change in liquid flow speed on the programmed structural array, we discharged liquid (water colored in red) from the left end of the microchannel, as shown in the movie cuts in **Figure 3-4b**. As shown in the graph of the liquid front position as a function of time, we could easily vary the fluid speed in a particular region within a channel by simply changing the orientation of a ratchet structure. In the regions A and C, the average velocities of liquid flow are about ~ 13.9 μm/sec and ~14.6 μm/sec, respectively while the flow velocity increases to ~ 47.4 μm/sec in the region B. The difference in the flow speed is due to the difference in the net forces on different contacting surfaces.(*74, 77, 80-82*) The results shown in the present study clearly lay a firm foundation to control the flow speed within microchannels simply by changing the direction of asymmetric ratchet orientation.

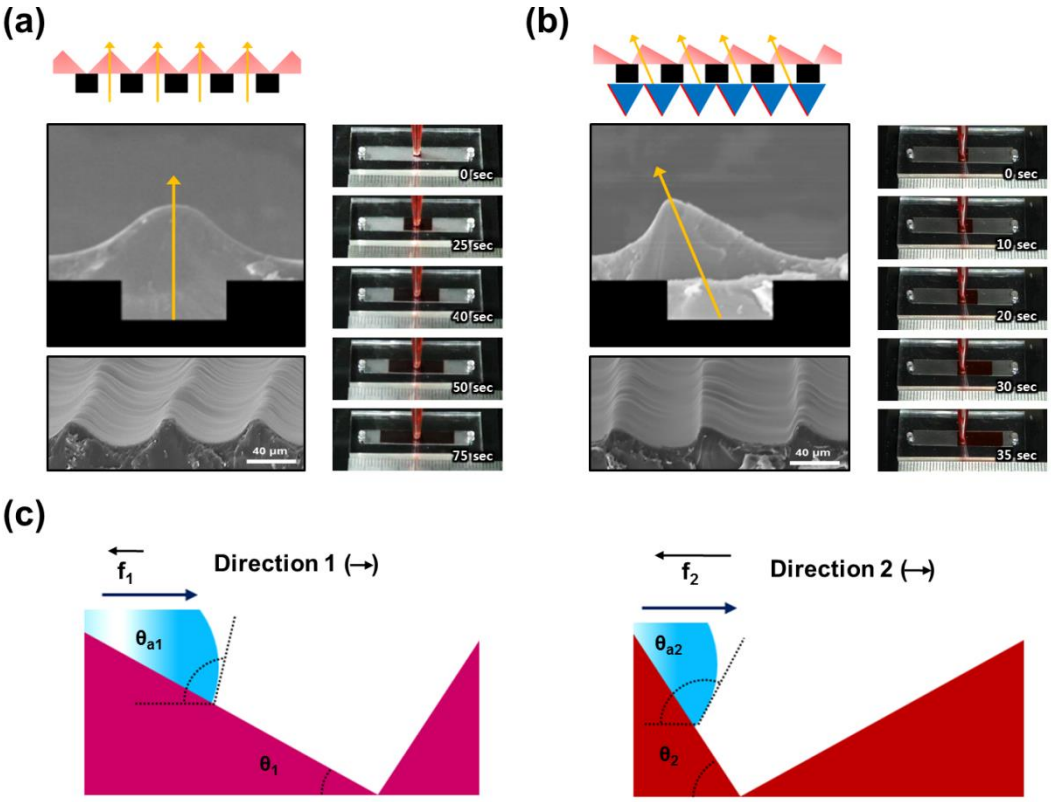

Figure 3-1. SEM images of polymeric structures realized within microchannels after UV illumination and representative movie cuts showing the liquid flow on the structures created within the microfluidic channels. (a) A liquid flow on a symmetric triangular pattern fabricated without a Lucius prism array. (b) A unidirectional liquid flow on an asymmetric ratchet realized with a Lucius prism array. (c) A simplified model to explain the flow velocity difference by the resistant retention force depending on contacting surfaces with different base angles.

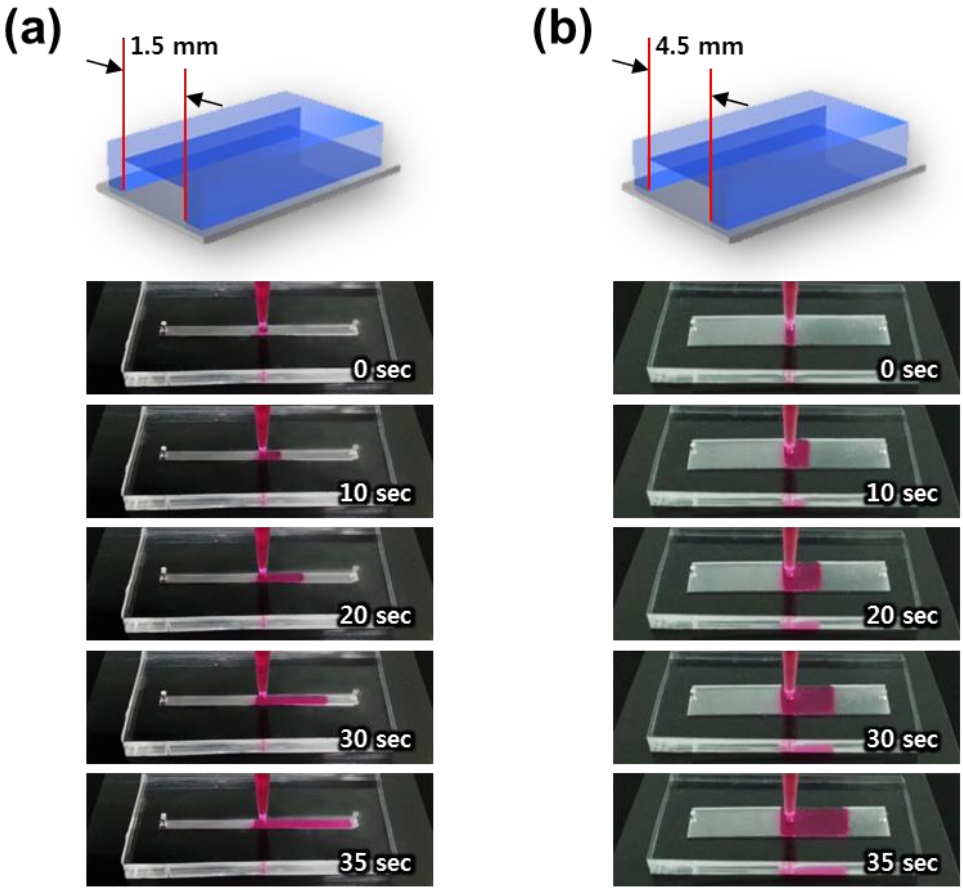

Figure 3-2. Movie cuts showing directional liquid flows within the microchannels of two different widths: 1.5 mm (a) and 4.5 mm (b).

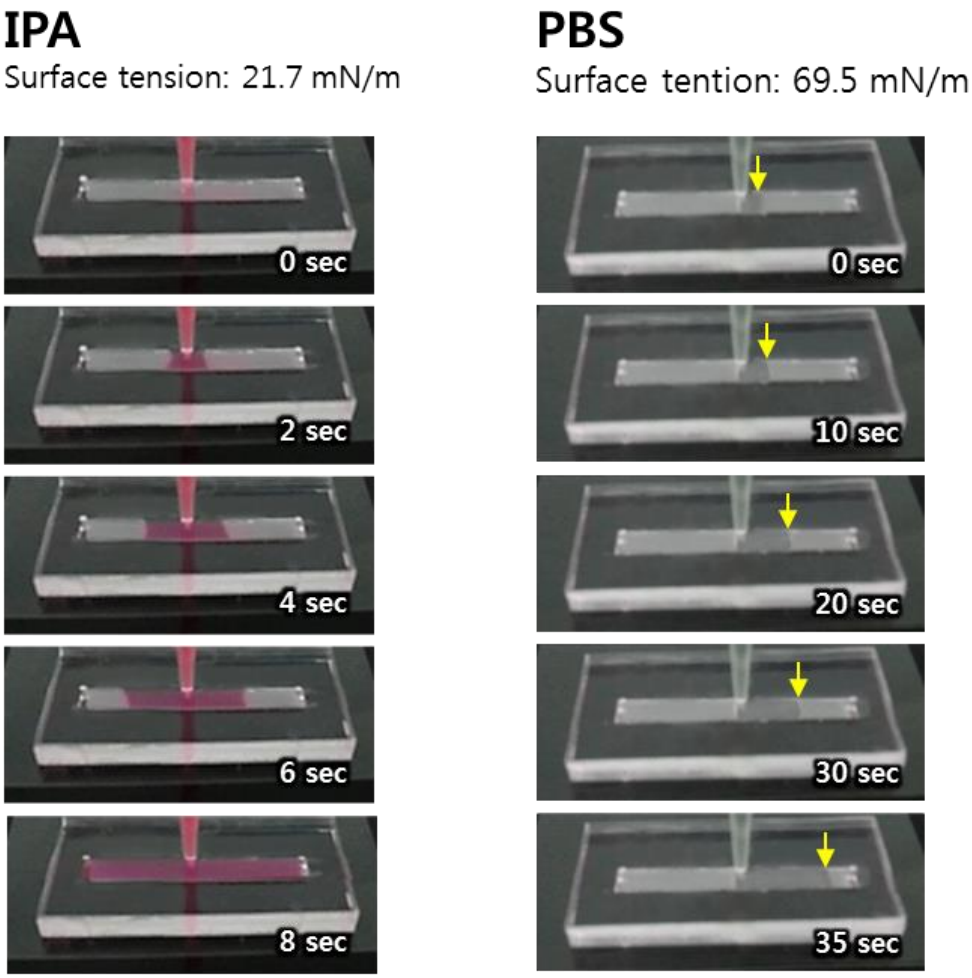

Figure 3-3. (a) Movie cuts showing a bi-directional flow of IPA (surface tension of 0.0217 N/m^2) (a) and a directional flow behavior of PBS solution (surface tension of 0.0695 N/m^2). It indicates that the directional behavior could be observed when the surface tension of liquid is high enough.

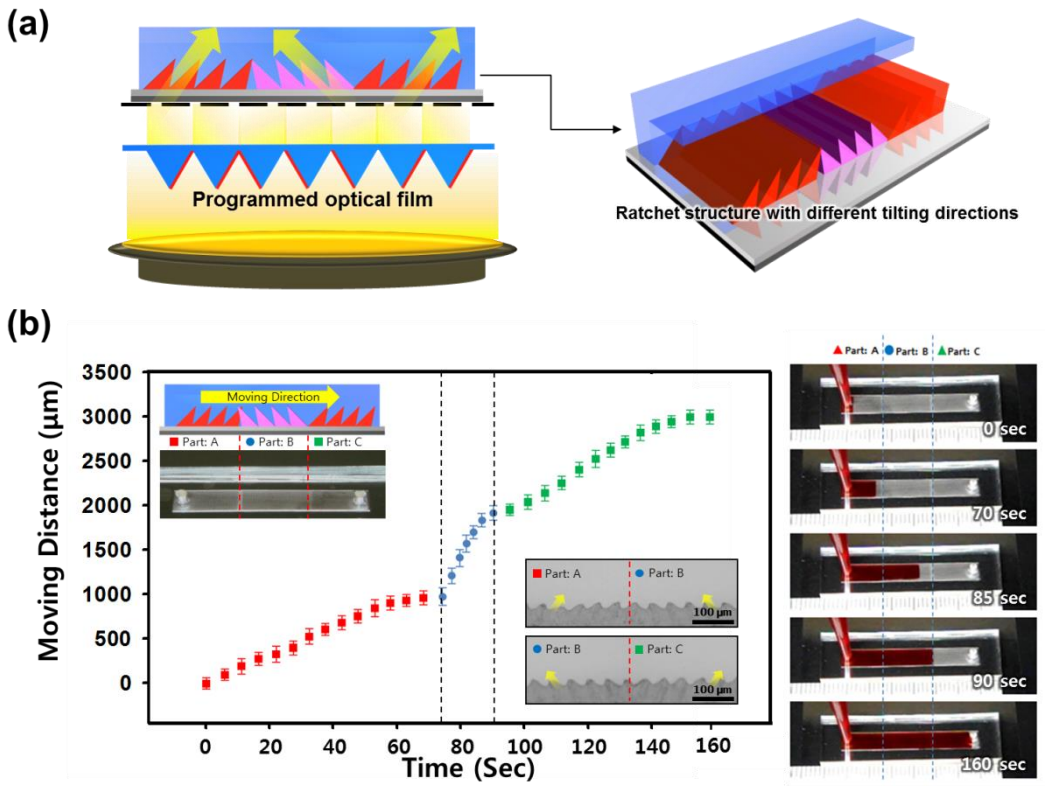

Figure 3-4. (a) A schematic illustration of programming the direction of asymmetric ratchet structures by a modified Lucius prism array. (b) The control of liquid flow velocity by the ratchet orientation along with representative movie cuts. The graph demonstrates the change in liquid flow velocity on the programmed asymmetric structures. (Insets: a schematic of asymmetry of ratchets of different regions and microscopic pictures of interfaces)

The second demonstration of the direct realization of rachet structures with different orientations is a microchannel of three pathways with different timings of fluid flow. For time-dependent assays including immunoassays or enzymatic reactions, delayed fluid flow could be effectively used in the aspect of time-dependent fluid injection.(*73, 83, 84*) To demonstrate the delayed fluid flow, a fluid (water mixed with red dyes in this case) was injected into three pathways with different asymmetric structures within a channel, as shown in **Figure 3-5**. To conduct experiments for the delayed fluid flow, a microchannel with three pathways was prepared through the conventional photolithography process. To realize three different asymmetric structures in different microchannel pathways of regions 1 to 3, we designed a Lucius prism array with programmed ratchet directions in three different pathways. In the region 1 (**Figure 3-5**), the guided transmission of light realized the asymmetic ratchets to the direction of smaller resistance. Also, the asymmetric ratchets in the reverse direction (region 3) and symmetric ratchets (region 2, w/o a Lucius prism array) were formed at the same time. Three different pathways with three different ratchet orientation angles, realized within a microchannel, demonstrate the controlled fluid wicking behavior. We observed the first fluid flow to region 1, followed by the flow into region 2 with symmetric ratchets with a time delay of 50 sec. After reaching the regions 1 and 2, the fluid flow finally switched to the region 3 with the highest resistant force with a time delay of 100 sec, as shown in **Figure 3-5**. The delayed fluid flow

in a programmed microchannel system could be useful in comparison with the previous trials employing surface treatment approaches(*73*, *83*) in terms of facile and economic fabrication of microchannels.

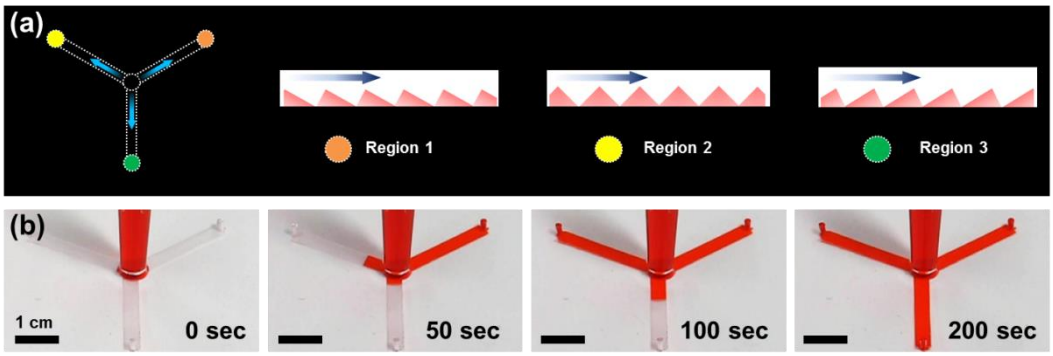

Figure 3-5. An example showing the delayed fluid flow based on different ratchet structures created within a microchannel. (a) A schematic illustration on differently oriented ratchet structures in three different channel regions. (b) Movie cuts showing the delayed fluid flow induced by different ratchet structures. In good agreement with the previous experimental results of controlled liquid flow velocity, injected liquid sequentially reached the regions 1, 2, and 3 with time lapse.

3-1-4. Summary

The asymmetric ratchet structures, created at the bottoms of microchannels, show the unidirectional liquid flows as well as controlling the fluid speed in a predefined region. Furthermore, we demonstrated two examples of asymmetric structures created or programmed in specific regions within microchannels to control the fluid speed in predefined regions and to be used as on-chip timers in split microchannels.

3-2. Thermoresponsive Switching of Liquid Flow Direction on a Two-Face Prism Array

3-2-1. Introduction

Recently, directional wetting and flow of liquid has received much attention for its potential use as a way of controlling liquid flow in microfluidics and water harvesting.(*60-67, 74, 80, 85-96*) Previous studies have mostly dealt with unidirectional liquid wetting or spreading on asymmetric microstructures. In one approach, inclined nanostructures in the form of stooped nanopillars(*62, 63, 65*) or inclined nanorods(*64, 67*) have been utilized for the unidirectional wetting. In others, the directional liquid spreading has been made possible with spatial gradients or anisotropic structure. (*60, 61, 66, 74, 80, 85-96*)

A basic question we raised regarding the unidirectional spreading and wetting is whether the unidirectionality can be made reversible with the same structure. That is to say that if the spreading is unidirectional in one direction on a given structure, could we make it unidirectional in the opposite direction on the same structure? A related intriguing question is whether this reversibility can be realized on demand. Directionality necessarily requires the anisotropy in terms of structure or gradient. (*60-67, 74, 80, 85-96*) The very nature of anisotropy, so much relied on for directionality, negates its use for the reversible directionality.

For the reversibility, therefore, a macroscopic, left-right symmetry in structure is needed. On the other hand, there has to be a force acting on liquid for the liquid front to advance in the desired direction. Within the overall symmetry, therefore, an anisotropy is needed to generate such driving force.

To address these issues, we present herein a designed structure with physical symmetry and chemical asymmetry for reversible and unidirectional step flow of liquid. The resulting structure is an array of equilateral triangular micro-prisms consisting of thermo-responsive polymers, only one face of which is covered with metal films (i.e., a two-face prism array). Because of the difference in the critical contact angle on the two surfaces, the liquid flows unidirectionally and the direction could be switched by exploiting the changes in wetting properties on thermo-responsive polymers with the control of temperature.

3-2-2. Experimental

Fabrication of the PNIPAAm patterned prism array

The masters used in the present study were prepared mechanically. First, a blank roll or plate of stainless steel electroplated by nickel was prepared. The blank roll or plate surface was machined by a diamond-cutting tool with a specific angle. In this process, the pitch and angle of carved patterns correspond to those of the diamond tool. The height of the patterns depends on the cutting depth of the diamond tool. In this study, prism master with 50 μm in period and 45° in prism angle was used. After the preparation of the master, a mixture of base and curing agent (10:1 w/w) of Sylgard 184 PDMS elastomer was poured onto the patterned masters and cured at 70 ℃ for 2 h. The cured PDMS molds were peeled off from the master and cut prior to use. Drops of a PNIPAAm prepolymer solution (mixture of N-isopropylacrylamide (NIPAAm), N,N-methylene-bis-acrylamide (MBAAm), ethanol, and 2-hydroxy-2-methylpropiophenon as a photoinitiator, with the weight ratio of 20:1:30:1) prepolymer solution were dispensed onto the prism shaped polydimethylsiloxane (PDMS) mold, and a flexible PET film, ~50 μm thick, was placed on top of the mould and lightly pressed against the moulding liquid (PNIPAAm) for a supporting backplane. The PNIPAAm liquid was then exposed to ultraviolet light for 10 min, with an intensity of 5.5 mW/cm^2 (Minuta Tech.). Subsequently, the cured polymer replica was removed from the

master.

Oblique metal deposition

The polymer prism array (50 μm in period, 45° in prism angle) was coated with ~20 nm thick Pt metal on one side of the prism using only oblique metal evaporation. We used a magnetron sputter for the metal deposition and placed the polymer prism array on an inclined holder with an angle 60°. The inclined holder defines the oblique incidence angle, resulting in the deposition of metal layers only on one side of the prism array. The two-face prism array thus fabricated had an area of 3 × 3 cm^2 and was cutted to a narrow strip of ~1.5 mm in width.

Physical measurements

Magnified optical images through two-face prism array was seen using an optical microscope (Olympus IX70, Japan). SEM images were taken using FESEM (Hitachi S-48000, Japan). Liquid flow movie cuts on a two-face prism array were obtained by a contact angle analyzer (KRUSS DSA 100, Germany).

3-2-3. Results and Discussion

The procedure involved in fabricating a two-face prism array is schematically shown in **Figure 3-6a**. To switch the chemistry of the surfaces, we used ultraviolet (UV)-curable poly(N-isopropyl-acrylamide) (PNIPAAm), which is a well-known thermo-responsive polymer(*97-105*) that switches from hydrophobic to hydrophilic below its Lower Critical Solution Temperature (LCST) of ~32 ℃. The prepolymer solution to fabricate the PNIPAAm prism structures was prepared by a mixture of N-isopropylacrylamide (NIPAAm), N,N-methylene-bis-acrylamide (MBAAm), ethanol, and 2-hydroxy-2-methylpropiophenon as a photoinitiator, with the weight ratio of 20:1:30:1.(*103, 104*) The liquid prepolymer was dropped onto a prism shaped polydimethylsiloxane (PDMS) mold and an original master to replicate the PDMS mold had been prepared by mechanical machining.(*55*) After crosslinking by 10 min exposure of UV (5.5 mW/cm^2, Minuta Tech.), a cured PNIPAAm prism array was detached from the PDMS mold, and thin platinum (Pt) metal films of ~20 nm were then deposited on only one face of the prism by the oblique deposition.(*55, 106-110*) **Figure 3-6b.** shows a scanning electron microscope (SEM) image of the two-face prism array used here. As seen from **Figure 3-6b**, the period is 50 mm with a typical prism angle of ~ 45° at both.(*55*) A magnified view in the inset of **Figure 3-6b** and an optical microscope image in **Figure 3-6c** demonstrate that the prism has the structural

symmetry in microscale and, at the same time, the chemical asymmetry due to the metal films selectively deposited on the left faces of the prism array.

To demonstrate the directional liquid flow on the two-face prism array, we placed a water droplet on the structure and increased the liquid volume at a constant feeding rate of 1 μl/min. **Figure 3-7a** shows the movie cuts of liquid flow moving toward the right direction. Interestingly, the liquid flow shows the step-wise movement with typical stick-slip behaviour,(*63*) as shown in the insets of **Figure 3-7a**. The magnified images demonstrate that the wetting can be described by the Wenzel state because the liquid droplet fills the entire micro-prism arrays. As the volume of water droplet is increased, the moving liquid front becomes pinned at the ridge until the liquid droplet overcomes the energy barrier against the movement. Then, the water front quickly steps over the ridge to the next prism valley, being pinned again. Such a cycle of pinning and step-over is repeated for the flow across the ridges of channels created by the prism array. In this sense, the unidirectional flow presented here could be termed as the "step flow". The characteristics of this step flow are shown in **Figure 3-7a**. It is noted that the water front moves unidirectionally toward the metal-free PNIPAAm surface.

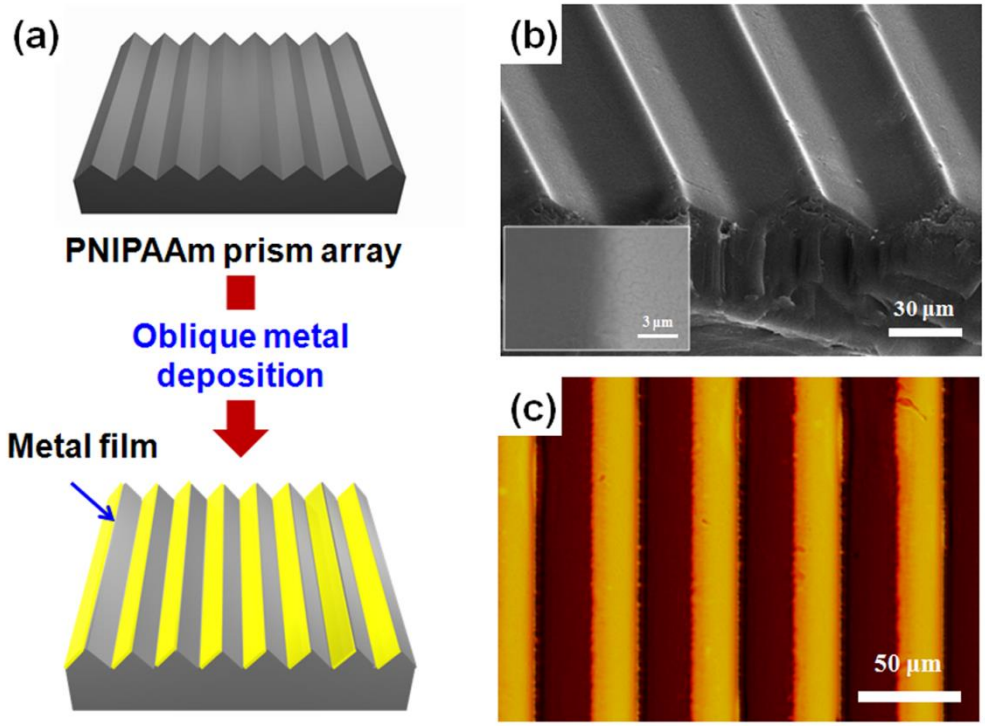

Figure 3-6. (a) A schematic illustration for the fabrication of a two-face prism array. (b) SEM image of a prism array showing the symmetric structure in microscale. The inset shows a magnified SEM image of the prism array with chemical asymmetry. (c) An optical microscope image showing the left faces of the prisms are covered with metal films.

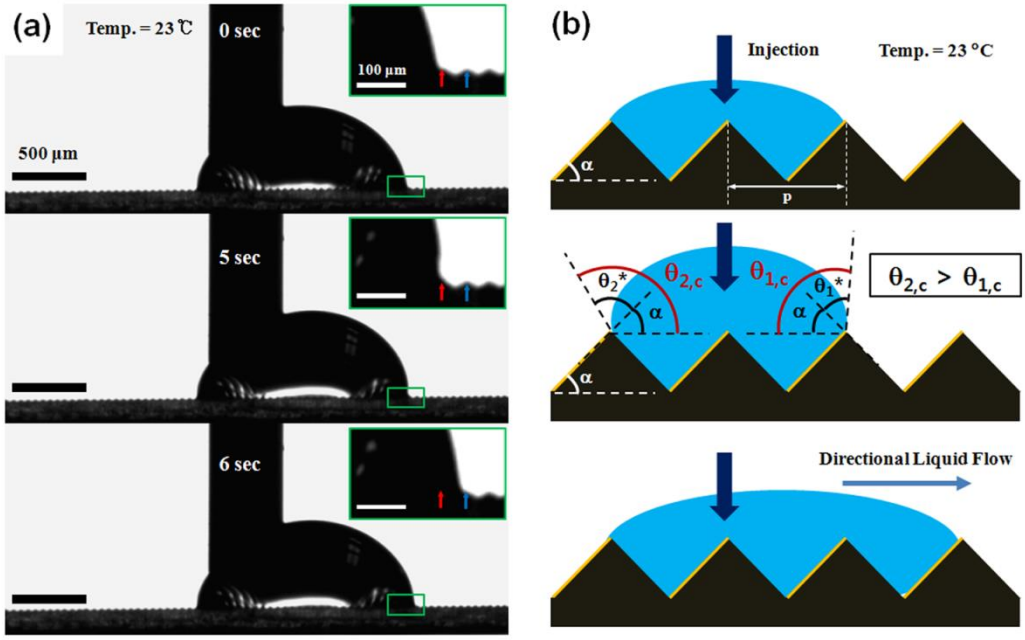

Figure 3-7. (a) Movie cuts at various times showing the unidirectional liquid step flow. The water front is moving unidirectionally toward the metal-free PNIPAAm surface (right face). It is noted that the black column on the liquid is a needle of the equipment for feeding water at a constant rate. The inset in each image shows the corresponding magnified image at the three-phase contact line where the colored arrows indicate the location of ridges. (b) A schematic illustration explaining the mechanism of the directional step flow across channels formed by the prism array.

Figure 3-7b is a schematic illustration of the mechanism involved in the directional liquid flow, with the three-phase contact line across the ridges of channels created by the prism array. As discussed earlier, the moving liquid front is pinned at the channel ridge and the pinning is maintained even in increasing the liquid volume until the contact angle of the liquid front reaches its critical contact angle at the edge. The critical contact angle qc can be written as follows:(*77, 78*)

$$\theta_c = \theta^* + \alpha \quad (1)$$

where θ^* is the equilibrium contact angle on a planar surface or the intrinsic contact angle and a is the angle subtended by the two prism surfaces forming a solid edge, which is referred to as the edge angle. θ_1^* is the contact angle on a planar PNIPAAm surface (right face) and θ_2^* is the angle on a metal-deposited planar surface (left face) In the two-face prism system, the critical contact angles of the two faces are different from each other because of their different surface chemistry. As a result, the critical contact angle is higher on one side or one face (i.e., the left side of the prism array in **Figure 3-7b** in the current case) than that of the other and the liquid front is forced to move in the direction of lower critical contact angle (i.e., the hydrophilic PNIPAAm surface in this case) as the liquid volume is increased.

It is well known that the liquid flows spontaneously and preferentially along the sidewalls of grooves or channels.(*77, 78*) A distinct difference in our work is that the liquid moves across or over the ridges of prism channels by

cutting the prism sheet to a narrow strip of ~1.5 mm in width. In this way, the liquid flow can be confined within the strip (direction 1 or 2 in **Figure 3-8**). Such a confined flow is beneficial for the controlled one-dimensional directional flow since the liquid front cannot spill over the lateral edges. Namely, the critical contact angles at both sharp edges are always higher than the other two critical contact angles at the channel ridges (i.e., angle of the sharp edge is 90˚).

To change the direction of the lower critical contact angle, we employed the reversible switching of wetting properties on thermo-responsive polymers, PNIPAAm, which switches the surface properties from hydrophobic to hydrophilic due to the competition between intermolecular and intramolecular hydrogen bonding below and above the LCST.(*97-105*) **Figure 3-9** shows the changes in CA on flat PNIPAAm and Pt-deposited surfaces with temperature cycles between 23 ℃ to 40 ℃. As shown in **Figure 3-9a**, the CA on the flat PNIPAAm surface is reversibly changed from ~45.4˚ (± 1.5˚) at ambient temperature (~23 ℃) to ~72.0˚ (± 2.0˚) at ~40 ℃ (above the LCST of ~32 ℃)) without additional chemical treatment. In contrast, almost a constant CA of ~61.4˚ (± 1.4˚) was observed on the Pt-deposited surface regardless of temperature cycles. As shown in **Figure 3-9b**, the CA on the Pt-deposited surface is located between the CAs on the PNIPAAm surface at temperatures below and above the LCST. When applying the temperature-dependent CA change to the two-face prism array, the PNIPAAm surface (right face) can exhibit lower or higher critical CA (θc)

than the CA of the Pt-deposited face (left face) depending on the substrate temperature. By utilizing these unique wetting characteristics of the two-face prism array, we could switch the direction of the lower critical CA by changing the substrate temperature.

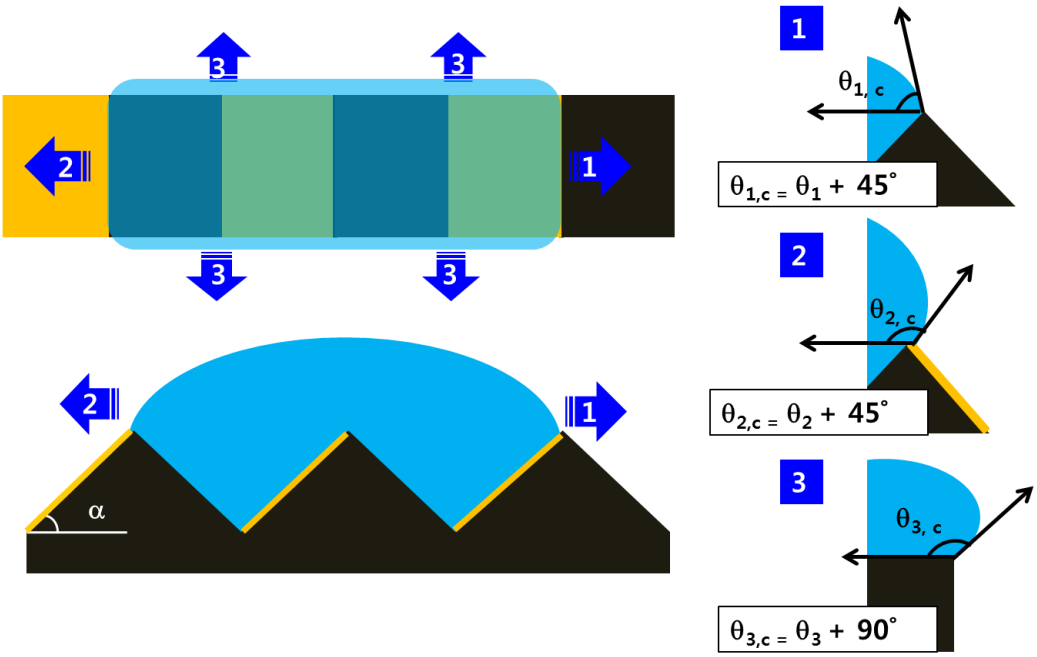

Figure 3-8. Schematic illustrations explaining the relationships of critical contact angles for three directions. Direction 1 means that a liquid droplet flows across the ridge of PNIPAAm surface. Direction 2 is toward the Pt-coated direction. Direction 3 is out of the prism array. Because the critical contact angle could be obtained by $\theta_c = \theta^* + \alpha$, the edge angle is very important to critical contact angle. In the case of direction 3, α is 90° and the critical contact angle $\theta_{3,c}$ is always higher than the lowest critical contact angle.

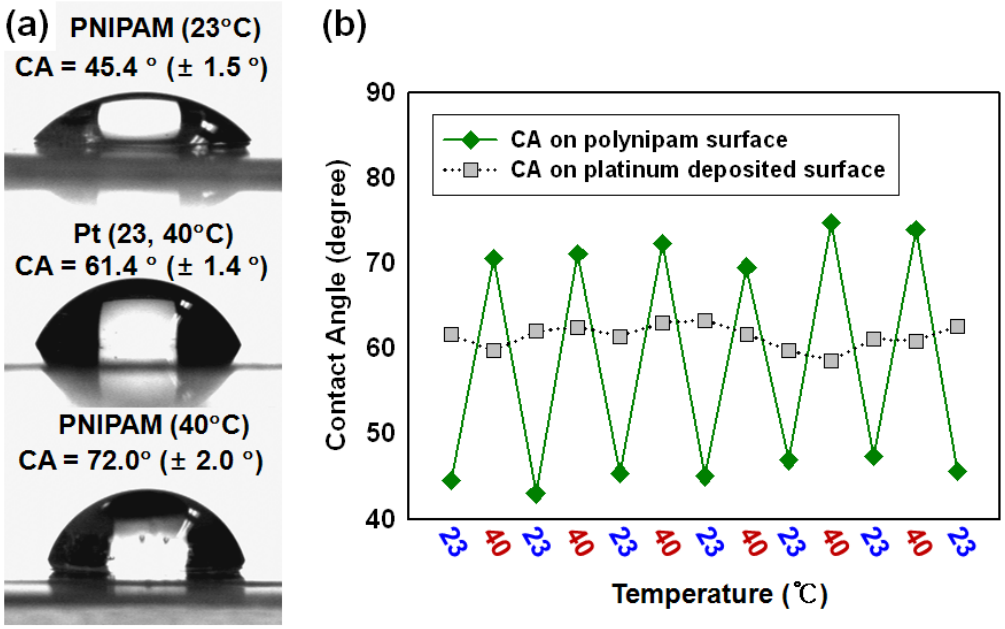

Figure 3-9. (a) Images of water droplets on PNIPAAm and Pt-coated surfaces under two temperature conditions (23 and 40 ℃). The contact angle (CA) on the PNIPAAm surface changes from 45.4˚ to 72.0˚ after the increase in temperature to 40 ℃ while the CA on the Pt surface remains at ~ 61.4˚ at both temperatures. (b) A graph showing reversible switching of CA on the PNIPAAm surface with temperature cycles along with CA variations on the Pt-coated surface.

Figure 3-10a shows a schematic illustration for the change in the direction of liquid flow on the two-face prism array at two dif*f*erent temperatures of 23 and 40 ℃. At 23 ℃, the liquid flows towards the PNIPAAm face (right direction) at a feeding rate of 6 μl/min with the lower critical contact angle of ~ 91.8 ° (theoretical value: ~90.4 °) (**Figure 3-10b**). Remarkably, the direction of the liquid flow was reversed towards the Pt-deposited face (left direction) when the substrate temperature was switched to 40 ℃. In this case, the lower critical contact angle to the left direction was ~132.0 ° (theoretical value: ~117.0 °) as shown in **Figure 3-10c**. Due to the hydrophobic nature of the surface at higher temperature, the speed of liquid flow was decreased at the same feeding rate. Such a reversal of the flow direction was repeated more than five times, in good agreement with the expected wetting behavior. It is noted that the liquid flows in both directions on a symmetric PNIPAAm prism array, suggesting that the directionality is originated from the asymmetric nature of surface properties.

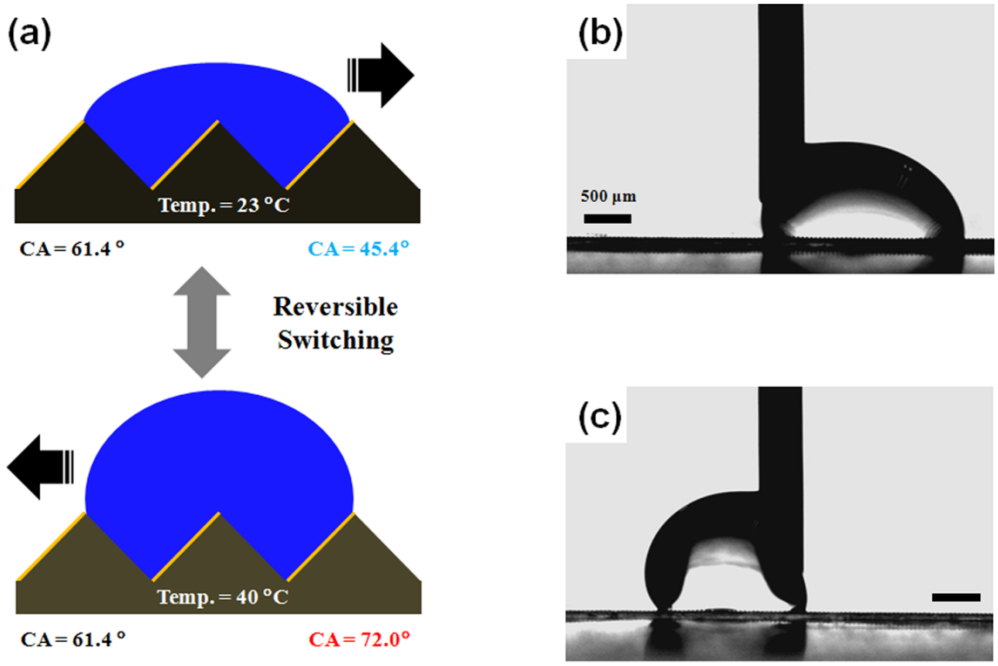

Figure 3-10. (a) A schematic illustration for the change in the direction of lower contact angle. (b) A movie cut showing the directional liquid flow on the two-face prism array at 23 ℃. Water flows toward the less hydrophobic, PNIPAAm surface with an apparent contact angle of ~90.9˚. (c) A movie cut showing the directional liquid flow at 40 ℃. The direction of liquid flow is reversed, toward the direction of Pt-deposited surface with an apparent contact angle of ~117.0˚. The same experiments were repeated more than five times.

3-2-4. Summary

We have presented a simple approach to reversibly switch the direction of liquid flow by temperature change with a thermo-responsive PNIPAAm structure. An array of micro-prisms, which is physically symmetric and chemically asymmetric, gives rise to unidirectional liquid flows across the ridges toward the lower critical CA. This allows the unidirectional “step flow” across ridges of prism channels. From the strategy to change CAs of thermo-responsive polymer surfaces, we could switch the direction of liquid flow reversibly by varying the substrate temperature. The reversible switching of a flow direction would be applicable to guide a flow in microfluidic devices without using closed channels (i.e., open channels) or harvest water in a more efficient way.

Chapter 4. Multiscale Architectures for Enhancing Performance in Polymer Electrolyte Membrane Fuel Cell

Published in Chemistry of Materials, 2013, 25, 1526 (*111*)

Published in doctorate thesis and reeditted

(Namgee Jung, 2012, Effects of catalyst surface structure on electrochemical property and catalytic activity in fuel cell, Seoul National University)

4-1. High Performance Hybrid Catalyst with Selectively Functionalized Carbon by Temperature-Directed Switchable Polymer

4-1-1. Introduction

Proton exchange membrane fuel cell (PEMFC) has been developed as an energy conversion device for the future due to its high efficiency and continuous production of the electricity by simply refilling hydrogen as a fuel.(*26*, *112*) However, there are still some obstacles such as low activity of cathode catalyst for the oxygen reduction reaction (ORR),(*113*) water management such as flooding in the membrane electrode assembly (MEA),(*114*) catalyst poisoning by CO in the anode,(*115*) and so on. From the point of view of the fuel cell system, the water

management in the MEA is one of the most important things since PEMFC always involves in production and transport of water in the MEA. Especially, the tri-phase boundary, where catalyst, ionomer and gas pore intersect, can be blocked by water produced by the ORR in the cathode, which results in water flooding.(*32, 112*) If water is not well removed from the catalyst layer, it seriously inhibits the oxygen transport to catalyst surfaces in catalyst layer. In the polarization curve of PEMFC, the mass transfer overpotential much rapidly increases as the current density is high, and it becomes consequently the main reason for voltage loss during the PEMFC operation.(*32*)

In recent decades, many researchers have developed various technologies to reduce water flooding in the catalyst layer.(*28, 116-119*) The first one was the introduction of hydrophobic polymer particles into the cathode catalyst layer.(*28, 116, 117*) For instance, polytetraflouroethylene (PTFE) particles were inserted and mixed with carbon-supported metal catalysts in the catalyst ink preparation, and the catalyst layer with PTFE particles was formed,(*117, 120*) or inserted PTFE particles were dissolved and adhered to the catalyst surface through additional hot press procedure during the MEA fabrication.(*28, 116*) The second method was related to the pore formers such as carbonate.(*118, 119, 121*) Large gas pores to improve the oxygen and water transport could be formed by removing inserted pore forming agent into the cathode catalyst layer.

However, those methods have some critical problems despite of the

respective advantages. First of all, when hydrophobic polymers adhere to the catalyst surfaces by hot press procedure, they have nothing to do but randomly stick to the surfaces. Due to the random adhesion of polymer, metal catalyst surface, where the electrochemical reaction occurs, may be blocked as well as carbon supports, which results in a fatal decrease in the electrochemical active surface (EAS) of catalysts.(*117*) In addition, the insertion of hydrophobic polymer particles or pore forming agent into the catalyst layer makes the catalyst layer thickness increase, and finally the oxygen transport may become hard when the same catalyst loading is used in the MEA.(*117, 118*) To overcome above problems, a break-through for the water management in catalyst layer of PEMFC is fundamentally required.

In this communication, we propose a idea to reduce water flooding in the catalyst layer through the development of carbon-supported Pt (Pt/C) catalyst selectively functionalized by poly(N-isopropylacrylamide) (PNIPAM), which is able to reversibly switch between hydrophilic and hydrophobic property depending on the temperature.(*100*) Hydrophobic catalyst layer without a decrease in the EAS and an increase in the catalyst layer thickness can be achieved by using the selectively-functionalized Pt/C catalyst. To the best of our knowledge, it is the first try selectively-functionalizing the carbon surface despite the existence of metal nano-particle on the carbon support in PEMFC.

4-1-2. Experimental

Synthesis of Pt/C-PNIPAM.

40 wt.% Pt/C (Johnson Matthey) was dispersed with amine-terminated PNIPAM (Aldrich) of 0.04 mM in a solvent of pH 1.6, which was composed of isopropyl alcohol (IPA) (Aldrich) and $HClO_4$ (Aldrich). After the solution was well mixed for 1 hr, 1-ethyl-3-(3-dimethylaminopropyl)carbodiimide (EDC) (Fluka) of 0.04 mM was quickly introduced as a catalyst into the vigorously stirred solution for the amide reaction between –COOH of the carbon surface and $–NH_2$ of amine-terminated PNIPAM. The solution was washed through the filtration by excessive D.I. water after the amide reaction by EDC for 12 hr. Finally, the filtered Pt/C-PNIPAM was dried at 60 ˚C.

Membrane electrode assembly (MEA) preparation.

The MEAs were prepared with and without PNIPAM in the cathode. A catalyst ink for the cathode catalyst layer with PNIPAM was fabricated by mixing Pt/C-PNIPAM, 5 wt.% Nafion ionomer solution (Aldrich) (0.5 of N/C ratio) and IPA. Non-treated 40 wt.% Pt/C was used in an anode catalyst ink instead of Pt/C-PNIPAM. In the MEA without PNIPAM, the anode and cathode catalyst inks

identically had non-treated 40 wt.% Pt/C. The prepared catalyst inks were sprayed onto the anode and cathode parts of the Nafion 212 membrane (Dupont). Nafion 212 membrane was used after the pretreatment, in which the membranes were boiled in 3 % hydrogen peroxide solution, 0.5 M H_2SO_4, and D.I. water at 80 ˚C in order. The Pt loadings were equally 0.2 mg cm^{-2} in the cathodes and anodes of the MEAs, respectively. The catalyst-coated membranes (CCMs) were dried at room temperature for 12 hr, and sandwiched between the anode and cathode gas diffusion layers (GDLs, SGL 35 BC) without hot press process.

Physical analysis.

Field emission-scanning electron microscopy (FE-SEM) was conducted using a SUPRA 55VP (Carl Zeiss) to measure the thickness and structure of the cathode catalyst layers. Atomic force microscopy (AFM) was carried out to identify the surface structure and roughness of the catalysts. X-ray photoelectron spectra (XPS) were obtained from an Al Kα source (ESCALAB 250 XPS spectrometer, VG Scientifics). Binding energies were calibrated with respect to C (1s) at 285 eV. Experimental data were curve-fitted using XPSPEAK4.1 software. Atomic ratios of Pt oxidation states were estimated from the area of the respective Lorentzian-Gaussian peaks. The advancing and receding contact angles (CAs) of the surfaces with Pt/C and Pt/C-PNIPAM were measured at 20 and 70 ˚C when a

water droplet with total volume of about 20 μl was drawn in and out onto each cathode catalyst layer using a contact angle analyzer (KRUSS DSA 100). The contact angle hysteresis was calculated from the differences between the advancing and receding contact angles.

Electrochemical measurements.

Cyclic voltammogram (CV) was obtained at 100 mV s^{-1} between 0.05 and 1.0 V to compare the electrochemical active surfaces (EAS) of the prepared cathode catalyst layers. Humidified H_2 at 75 ˚C and N_2 at 70 ˚C were supplied to the anode and cathode, respectively. For the unit cell performance test, humidified H_2 (150 ml min^{-1}) at 75 ˚C and air (800 ml min^{-1}) at 70 ˚C were flowed into the anode and cathode, respectively. In fuel cell operation, unit cell temperature was 70 ˚C. Electrochemical impedance spectroscopy (EIS) (IM6, Zahner) of the unit cells was measured at 0.8 and 0.65 V with an amplitude of 10 mV. The measurement was conducted in a frequency range from 0.1 Hz to 10 kHz. Other experimental conditions such as temperature and gas humidification were the same as fuel cell operation. The ZView program (Scribner Associates, Inc.) was utilized to fit the EIS data, and a simple equivalent circuit was applied.

4-1-3. Results and Discussion

Switching property of hydrophilicity at each step is essentially required for particle dispersion at MEA preparation process and water management at PEMFC operation. The carbon support should have necessarily hydrophilic functional groups to uniformly disperse the catalyst of nanoparticles on the carbon surface when carbon supported Pt-based or other metal catalyst is synthesized.(*122, 123*) Therefore, the carbon support such as carbon black, carbon nanotube (CNT) and carbon nanofiber (CNF) are generally activated through the acid treatment to have the functional groups such as –COOH and -C=O on the surface, and the hydrophilic functional groups on carbon still remain after the catalyst synthesis. In addition, catalyst having a carbon support without the functional groups show bad dispersion in the catalyst ink,(*123-125*) and large catalyst agglomerates may be formed, which results in low Pt utilization in the MEA.(*126*) Therefore, the carbon surface needs to be hydrophilic because the catalyst has to be well dispersed in the catalyst ink, which consists of catalyst, ionomer and solvent, at a room temperature. On the other hand, from the point of view of the water management in the MEA, hydrophobic carbon surface is required for the prevention from flooding of the catalyst layer in operating PEMFC at ~70 ℃ since water can be accumulated on the carbon surface. In addition, oxygen gas can easily transfer to the Pt through the hydrophobic channel

on the carbon surface.(*117*) Accordingly, to satisfy the requirements of hydrophilicity depending on purposes from the catalyst synthesis to the PEMFC operation, the wetting property of the carbon surface should be tuned at each step. However, when one makes the carbon surface property changed from hydrophilic to hydrophobic, the selective functionalization technique is necessary since the carbon surface tuning go through with affection of Pt nanoparticles on the carbon. In addition, the material with different hydrophilicity according to the temperature is needed because a variable is only the temperature from a room temperature to ~70 ℃ at the moment requiring the surface property change.

It is known that PNIPAM exhibits thermally responsive switching hydrophobicity.(*103, 127-133*) This phenomenon comes from the competition between intermolecular and intermolecular hydrogen bonding below and above the lower critical solution temperature (LCST) of about 32 ℃. On account of the responsive behaviour, PNIPAM has been studied at broad research areas, such as tissue engineering,(*103, 127*) drug delivery,(*128, 129*) micro/nano actuators(*130, 131*) and sensors(*132, 133*) requiring to response to specific stimuli. Herein, we utilized the switchable wetting behaviour of PNIPAM in PEMFC to solve the dilemma, which was that the carbon support needed simultaneously hydrophobic and hydrophilic property, and introduced a simple selective functionalization technique.

Figure 4-1 shows the schematic illustration for the synthesis of

selectively-functionalized Pt/C (Pt/C-PNIPAM). Amine-terminated PNIPAM (NH2-PNIPAM) and functional groups (-COOH) on the carbon surface selectively formed the amide (-CONH) bond with a aid of 1-ethyl-3-(3-dimethylaminopropyl)carbodiimide (EDC) as a catalyst.(*134*)

The synthetic mechanism can give selectivity for the functionalization of the carbon surface despite the existence of Pt nanoparticle. The catalysts were properly agglomerated each other in the catalyst layer of the MEAs as shown in **Figure 4-2**. It implies that Pt/C-PNIPAM was able to be well mixed in the catalyst ink since PNIPAM was hydrophilic at a room temperature during the MEA preparation. However, the surface of Pt/C-PNIPAM seemed to be similar to that of non-treated Pt/C in the scanning electron microscope (SEM) images. To definitely identify the surface structure of the catalysts, the surface roughness of Pt/C and Pt/C-PNIPAM is additionally measured by atomic force microscopy (AFM). First of all, AFM image of Pt/C-PNIPAM seemed to be rougher than that of Pt/C, and the measured roughness of Pt/C and Pt/C-PNIPAM were 9.44 nm and 15.00 nm, respectively. It shows that PNIPAM may be well distributed among Pt nanoparticles on the carbon surface.

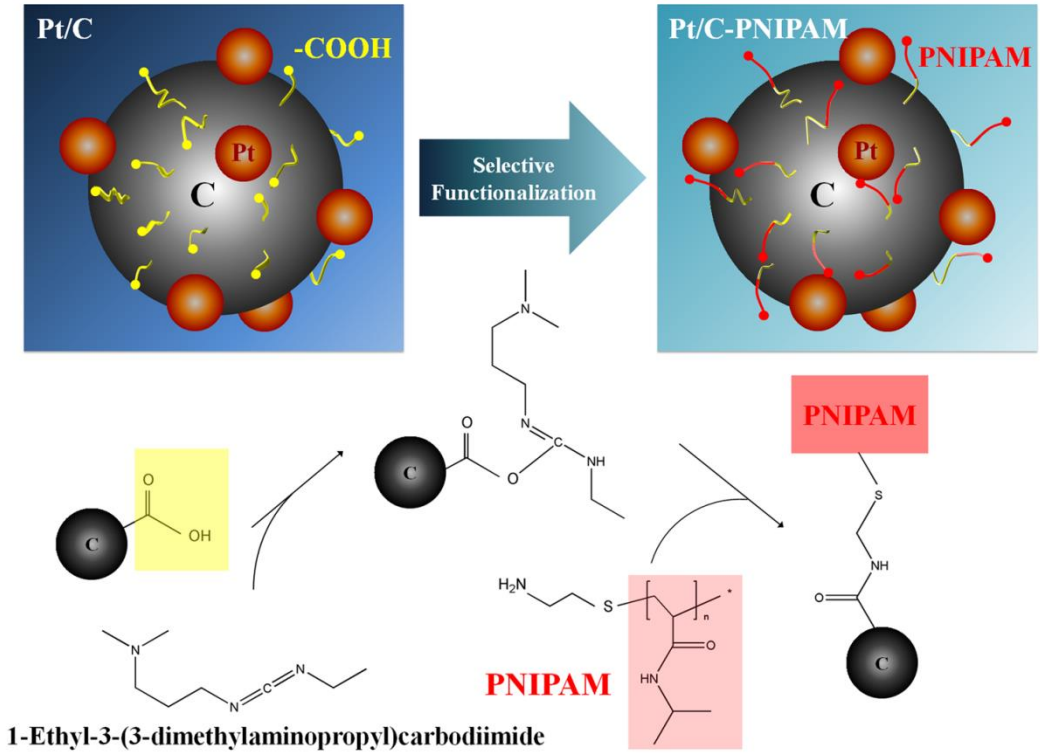

Figure 4-1. Schematic illustration of synthesis of selectively functionalized Pt/C (Pt/C-PNIPAM).

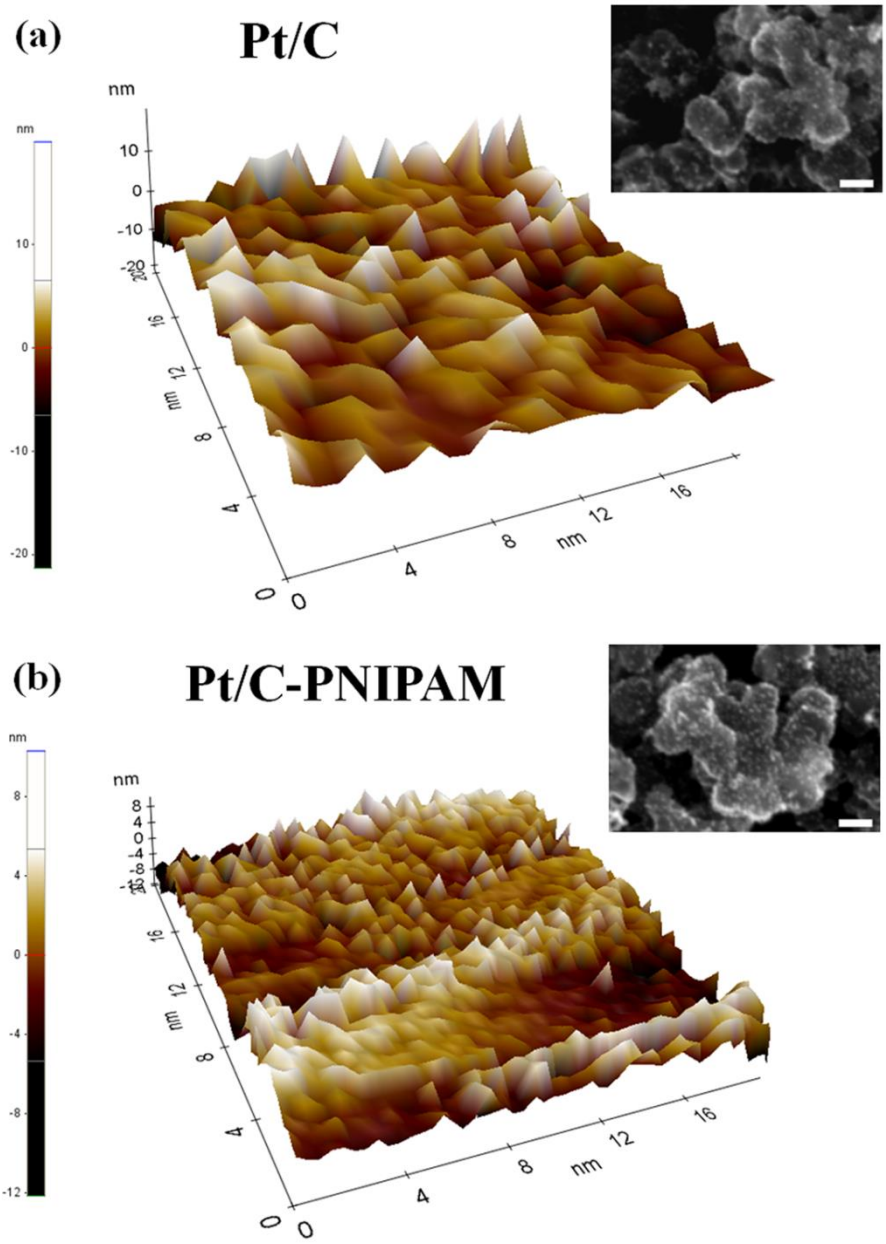

Figure 4-2. AFM images showing the morphology of each surface: (a) Pt/C, (b) Pt/C-PNIPAM. Each inset shows corresponding SEM images. (Scale bar: 50 nm).

For the characterization of the amide formation, X-ray photoelectron spectroscopy (XPS) was conducted and analyzed onto each catalyst surface. The existence of N 1s peak at 400.5 eV of Pt/C-PNIPAM shows that the amide bond was formed between the carbon surface and PNIPAM.(*135, 136*) (**Figure 4-3a**) In addition, it indicated that PNIPAM was selectively functionalized only on the carbon surfaces without affecting Pt surfaces. **Figure 4-3b** indicates that Pt 4f core-level peaks of Pt/C and Pt/C-PNIPAM were almost not changed, and the ratio of Pt oxidation states of Pt/C-PNIPAM was analogous to that of Pt/C. Especially, cyclic voltammograms (CV) of the cathode catalyst layers with and without PNIPAM were also similar to each other, and the EAS of Pt/C-PNIPAM calculated from the Hupd regions was analogous to that of Pt/C. (**Figure 4-4**a) From the analysis, it was elucidated that PNIPAM did not attach to Pt nanoparticles, and hardly affected the electronic structure of Pt. Therefore, the chemically synthetic method for carbon surface functionalization secured the selectivity. Successful thermal responsibility of PNIPAM on the carbon surface could be elucidated by measuring advancing and receding contact angles at ~20 ℃ (below LCST) and ~70 ℃ (above LCST) as shown in **Figure 4-5**. The catalyst layer with Pt/C had a similar and high contact angle hysteresis (= θ_a- θ_r) value at 20 ℃ and 70 ℃. It means that Pt/C may have strong water retention ability in the catalyst layer regardless of the PEMFC operating temperature. On the contrary, Pt/C-PNIPAM showed a contact angle hysteresis of very small value only at

70 ℃, which elucidates the catalyst layer with Pt/C-PNIPAM could become much hydrophobic in PEMFC operation at 70 ℃. The contact angle hysteresis data was the most critical factor to be sure of the utilization of PNIPAM on the carbon surface for the water management in PEMFC.(*137, 138*)

As shown in **Figure 4-6**, the MEA using Pt/C-PNIPAM as a cathode catalyst definitely showed much higher unit cell performance than that using Pt/C at 70 ℃. PNIPAM on the carbon surface affected the fuel cell performance exactly in the high current region related to water flooding. The PEMFC performance in the low current region was the same as that of Pt/C since Pt catalyst of Pt/C-PNIPAM was not affected by the selective functionalization of the carbon support. Though, in the high current region, the MEA with Pt/C-PNIPAM was possible to have high power density since water flooding was reduced by hydrophobic property of PNIPAM-functionalized carbon surface. Additionally, the semi-circles in low frequency region of the electrochemical impedance spectroscopy (EIS) indicated that the mass transfer resistance of Pt/C was larger than that of Pt/C-PNIPAM in **Figure 4-6**. When the EIS data was fitted and calculated by the equivalent circuit (**Figure 4-7a**), the Warbug impedance of Pt/C was much larger than that of Pt/C-PNIPAM although the current density Pt/C-PNIPAM was higher than that of Pt/C at 0.65 V. It means that the removal rate of water from Pt/C-PNIPAM was increased, and oxygen could rapidly access to the Pt catalyst through the hydrophobic carbon surface.

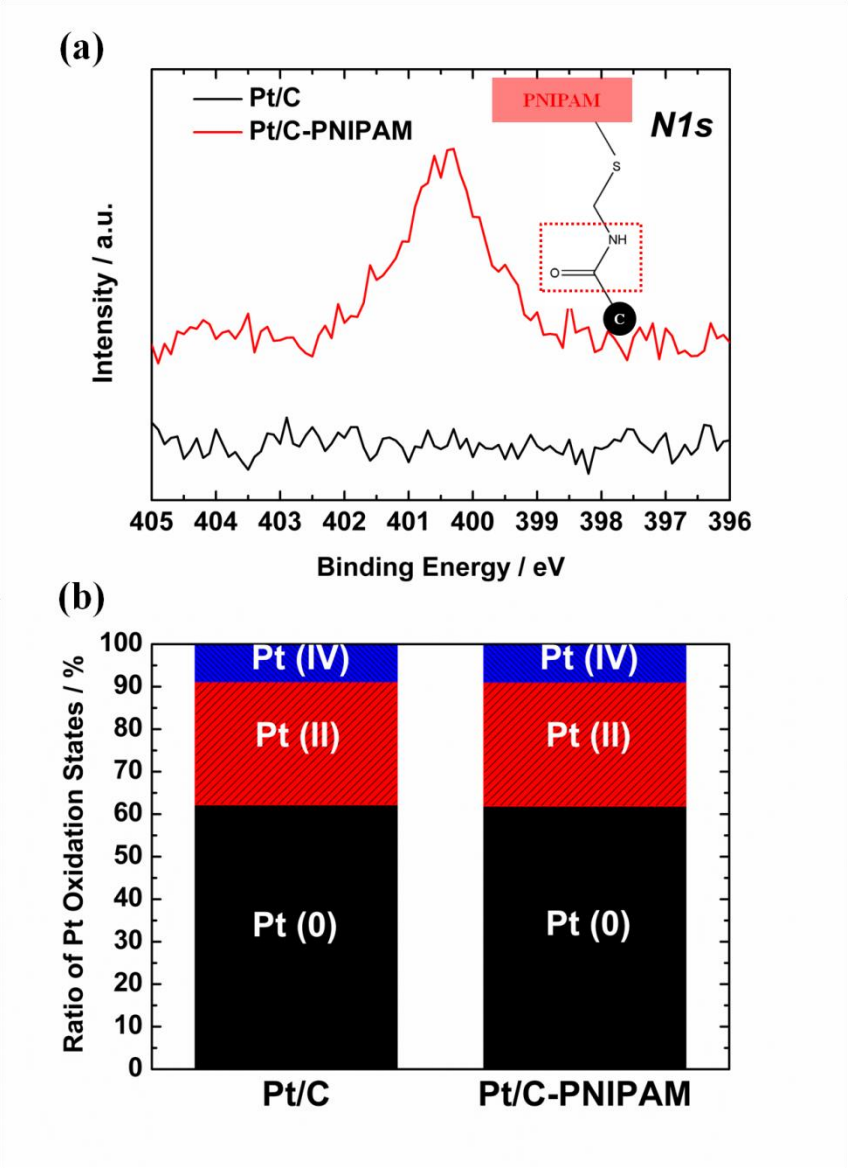

Figure 4-3. (a) N1s XPS peaks, and (b) ratio of Pt oxidation states in Pt/C and Pt/C-PNIPAM.

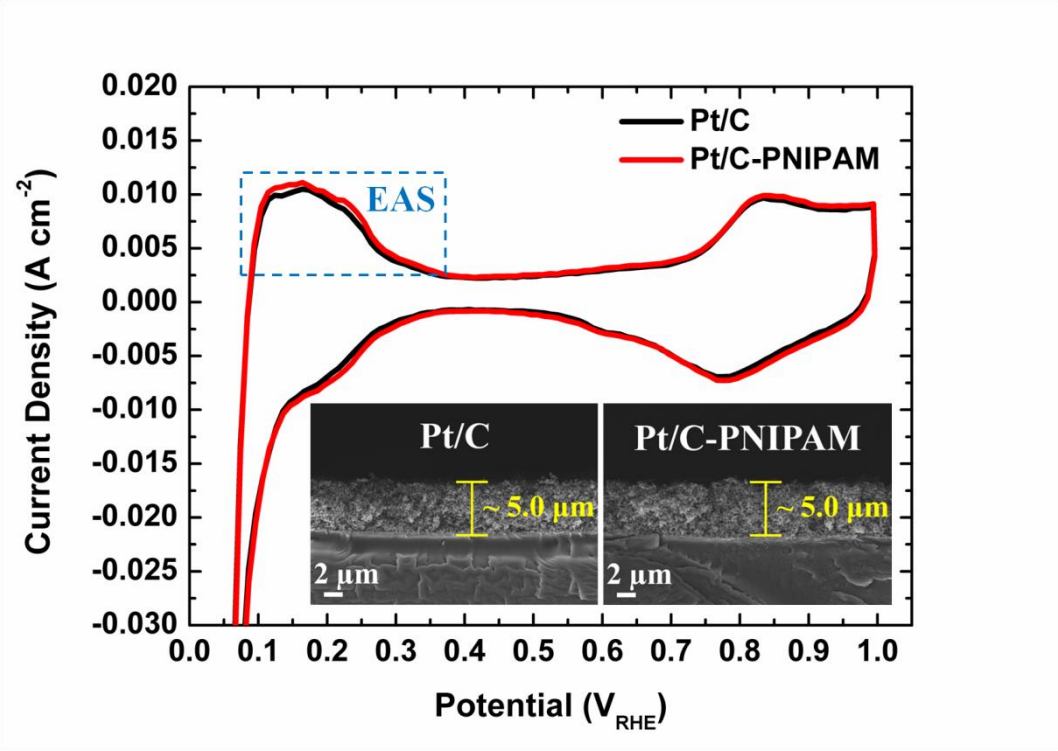

Figure 4-4. CV of the cathode catalyst layers with and without PNIPAM. Each inset indicates the SEM images showing the catalyst layer thickness of Pt/C and Pt/C-PNIPAM.

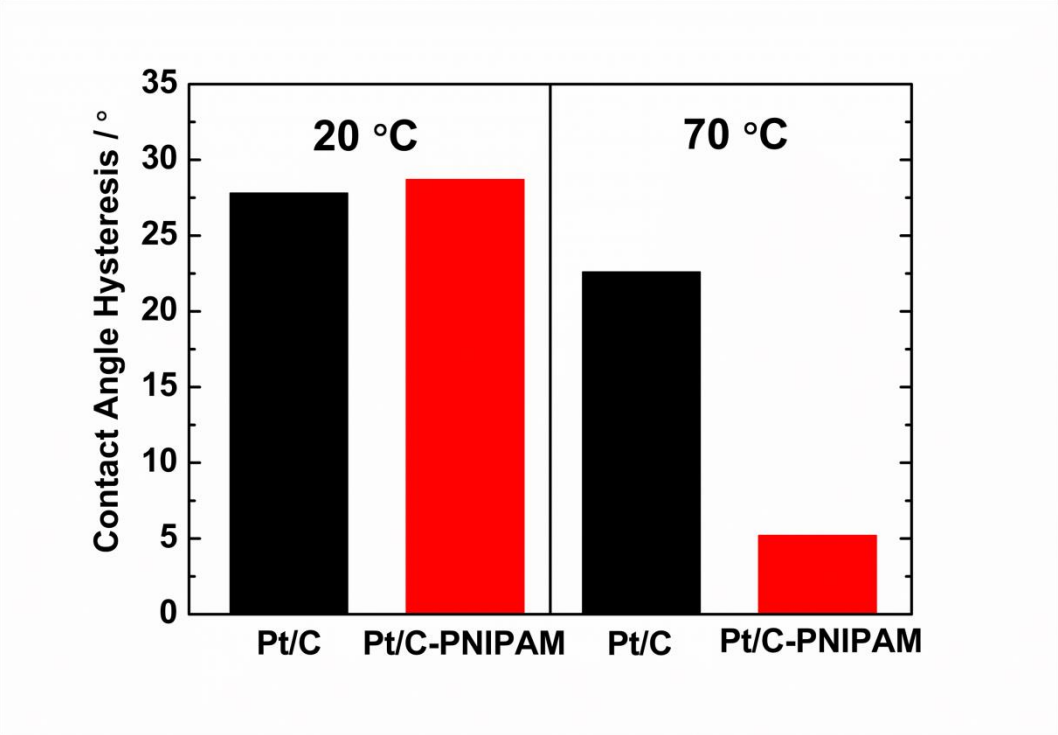

Figure 4-5. Contact angle hysteresis of surfaces with Pt/C and Pt/C-PNIPAM at 20 and 70 ˚C.

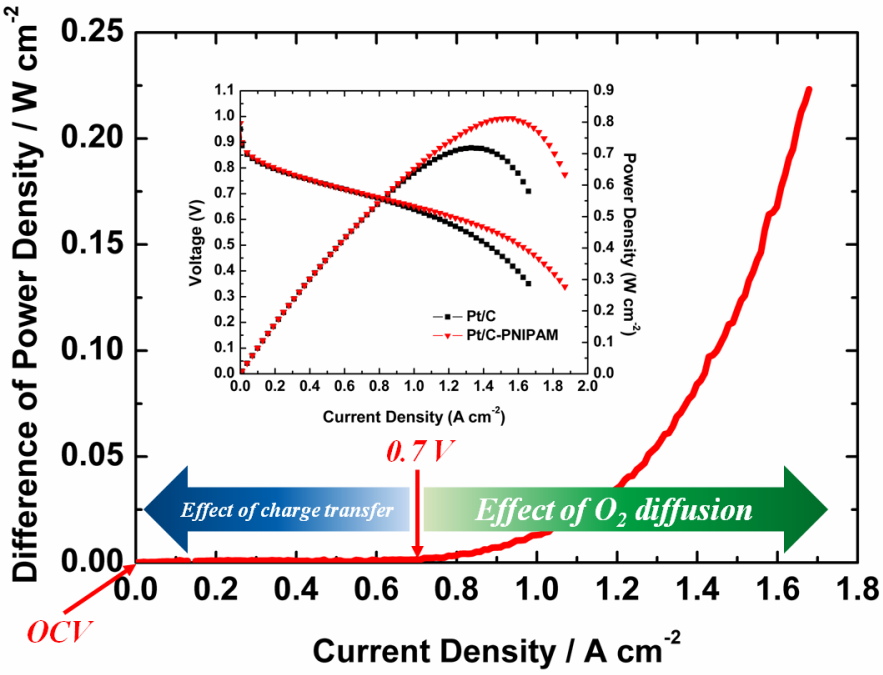

Figure 4-6. The difference between the power densities of the unit cells with Pt/C and Pt/C-PNIPAM according to the current densities. The inset shows the unit cell performance of the MEAs with Pt/C and Pt/C-PNIPAM.

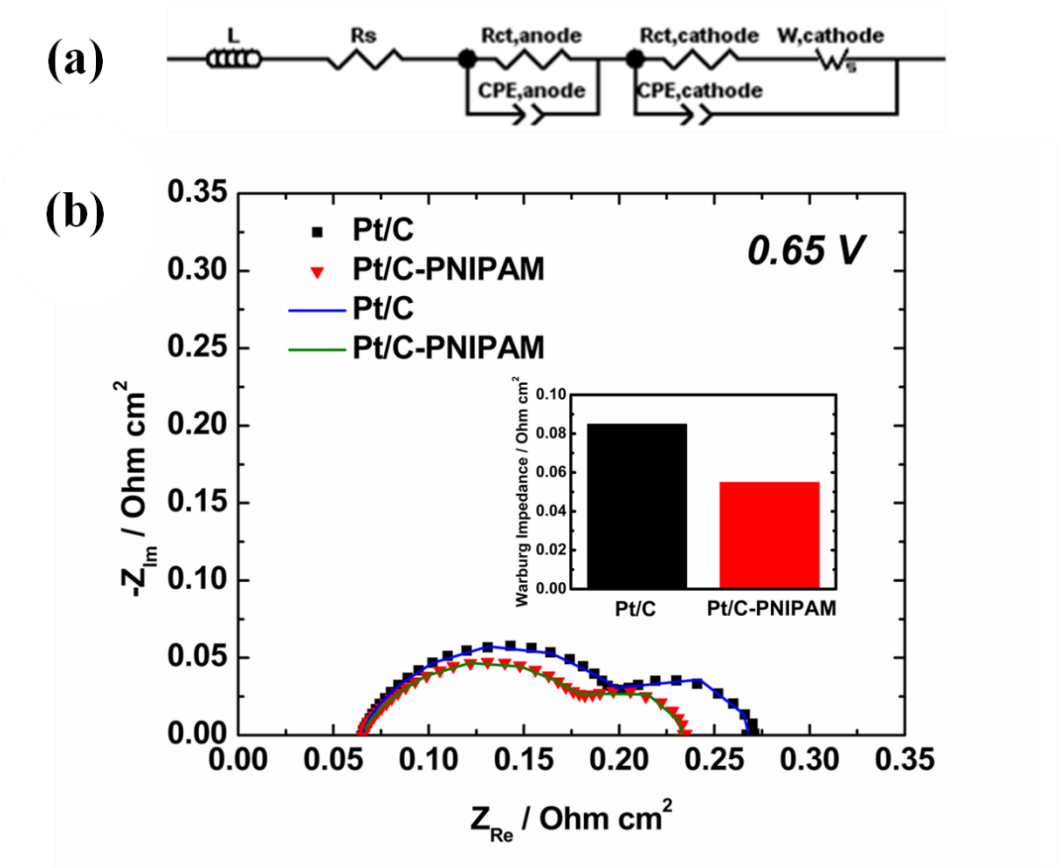

Figure 4-7. (a) Equivalent circuit of PEMFC. (L: inductance of wire, Rs: series resistance, R_{ct}: charge transfer resistance, CPE: constant phase element, W: Warburg impedance) (b) EIS of the MEAs with Pt/C and Pt/C-PNIPAM at 0.65 V. (Dot: raw data, Line: fitting data) The inset of (b) indicates the Warburg impedances calculated from the fitting data.

To understand the improvement of water transport in the catalyst layer with Pt/C-PNIPAM, we propose here simple theoretical model. A competition between systematic pressure as driving force (F_d) and adhesion force between solid-liquid interface as resistant force (F_r) might determine the extent of water transported through pores in the MEA. The MEA surface of Pt/C and Pt/C-PNIPAM is highly hydrophobic. Hence, pressure differential (ΔP) should overcome Laplace pressure (ΔP_L) to force water into pores.(*139*) The relation is expressed in force term as,

$$F_d \geq \Delta P_L A = \left(\frac{2\gamma_w|cos\theta|}{r_p}\right)\left(\pi {r_p}^2\right) = 2\pi r_p \gamma_w |cos\theta|, \qquad \theta \geq 90^\circ$$

, where γ_w is surface tension of water, r_p is radius of pore and θ is contact angle of pore surface.

When considering counterpart term, water transport is inhibited by adhesion of water on pore surface. The hysteresis in the adhesion energy (ΔW) between solid-liquid interfaces can be gained by measuring contact angle hysteresis.(*63, 137, 140*) Accordingly, the resistant force of water transport can be obtained as,

$$F_r = \Delta W l = \gamma_w(cos\theta_r - cos\theta_a)\left(2\pi r_p\right)$$

where θ_r is receding contact angle and θ_a is advancing contact angle.

For comparison, a term F_d divided by F_r is used to indicate the extent of water transport.

$$\frac{F_d}{F_r} \geq \frac{|cos\theta|}{(cos\theta_r - cos\theta_a)}$$

The right side value of Pt/C is 3.0, and that of Pt/C-PNIPAM is 18.4, which is increased by about six multiple. It indicates that Pt/C-PNIPAM was possible to easily remove water from the carbon surface in the catalyst layer. Therefore, the improvement of water management in the catalyst layer with Pt/C-PNIPAM can be explained by a simple mathematical model.

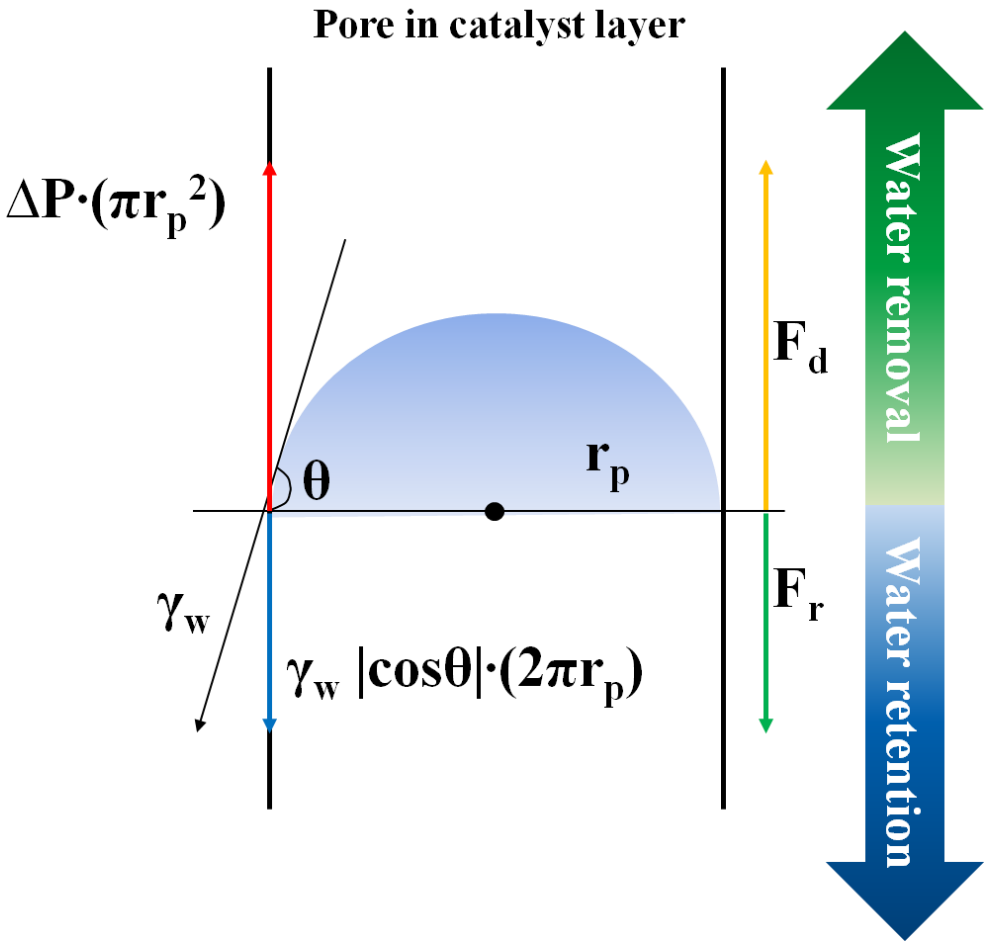

Figure 4-8. Schematic illustration of theoretical model to estimate the extent of water transported through the micro-pores in catalyst layer.

4-1-4. Summary

Pt/C catalyst was selectively functionalized by thermally responsive PNIPAM to give the carbon surface hydrophilic and hydrophobic properties simultaneously. During the MEA fabrication and PEMFC operation, Pt/C-PNIPAM was able to change its surface property according to required temperature. It was well mixed in the catalyst ink at a room temperature, and showed consistent unit cell performance in the low current density region without affecting Pt catalyst in the PEMFC operation. However, in the high current density region, hydrophobic property of Pt/C-PNIPAM made the power density much higher due to fast removal of water and rapid oxygen accessibility to the Pt surface in the catalyst layer. Consequently, it was confirmed that selective functionalization of the carbon support with thermally responsive polymer was successful for the water management in PEMFC. In addition, it is considered that the present synthetic idea and experimental results may provide a new insight for various energy device applications using organic and inorganic composite materials, functional polymer depending on the purpose.

4-2. High Performance Ultra-thin and Free-standing Multiscale Nafion Membrane via Enhanced Proton Conductivity with Increased Reaction Area

4-2-1. Introduction

Polymer electrolyte membrane fuel cell (PEMFC) has been studied as an environmental-friendly energy conversion device that provides high efficiency of electricity generation (*26*, *112*). Although there have been extensive studies for improvement of PEMFC performance such as developments of high performance electrocatalyst, membrane and novel structure of membrane electrode assembly (MEA), several technical challenges including the sluggish oxygen reduction reaction (ORR) and low utilization of catalyst in MEA have been remained for commercialization of PEMFC (*113*-*115*). Especially, Nafion membrane that selectively transport proton from anode to cathode has an critical effect on the performance in PEMFC relating to internal resistance. Of course, minimizing membrane thickness as possible in MEA is better to reduce the resistance resulting in higher performance (*33*). Nevertheless, adjusting membrane thickness is limted by several practical issues including mechanical strength, electrical short and fuel crossover (*33*). To address the above problem, a first trial of facile multiscale

approach to get thin membrane with high robustness and augmented triphase boundaries (TPBs) which are regions of electrochemical reaction, resulting in enhanced performance has been proposed.

4-2-2. Experimental

Preparation of multiscale Nafion membrane via thermal imprinting process.

Nafion membrane (Nafion 212, Dupont) was uniformly placed onto as-prepared multiscale PDMS mold and glass substrate. Then, the sandwich assembly was imprinted under hydraulic pressure (10~20 kg cm^{-2}) and temperature (~120 ℃) for 30 min. After cooling down to room temperature, patterned Nafion membrane were peeled off from the PDMS mold and keep Nafion membrane into deionized water container for ~12 hrs.

Membrane electrode assembly (MEA) preparation.

A catalyst slurries for the anode and cathode catalyst layer were fabricated by mixing 40 wt.% Pt/C (Johnson Matthey), Nafion ionomer solution and 2-propanol (Sigma Aldrich). Multiscale and flat nafion membranes (Dupont) were used after the pretreatment. They were boiled in 3 % hydrogen peroxide solution, and rinsed in D.I. water. After that, they were soaked in 0.5 M H_2SO_4, and washed again in D.I. water. Each procedure in the solutions was performed at 80 ˚C for 1 h, respectively. The prepared catalyst slurries were sprayed onto the anode and cathode parts of the Nafion membrane. The Pt loadings were equally

0.12 mg cm^{-2} in the anodes and cathodes of the MEAs, respectively. The catalyst-coated membranes (CCMs) were dried at room temperature for 12 h, and sandwiched between the anode and cathode gas diffusion layers (GDLs, SGL 35 BC) without hot press process. The active geometric areas of the MEAs were 5.0 cm^2.

Physical analysis.

Magnified optical images were seen using an optical microscope (Olympus IX70, Japan). Field emission-scanning electron microscopy (FE-SEM) was conducted using a SUPRA 55VP (Carl Zeiss) to measure morphology of the various sample used in this paper. The Fourier Transform Infrared Spectroscopy (FTIR) spectra were obtained using Vertex 70 with FT-IR spectrometer (BRUCKER). IR radiation was detected by a liquid-nitrogen-cooled mercury cadmium telluride detector. FT-IR data were obtained to monitor the degree of photopolymerization of PUA as a function of UV exposure time.

Electrochemical measurements.

For the single cell performance test at 80 ˚C, humidified H_2 and O_2 (air) gas were flowed into the anode and cathode, respectively. The stoichiometric

coefficient of H_2/O_2 (air) was 2.0/9.5 (2.0), with total outlet pressure of 150 kPa. Also, the RHs for the anode and cathode gases were 100 %. The proton conductivity (σ) of membrane is calculated using the equation, $\sigma = d/RS$, where d is the distance between the reference and sensing electrodes, and S is the cross-section area of a membrane.

4-2-3. Results and Discussion

For an evaluation of multiscale engineering that takes advantages of each micro/nanoscale structure at the same time, we constructed a multiscale polymer electrolyte membrane fuel cell (PEMFC) by incorporating multiscale architectures into Nafion membrane that selectively transport proton (H+) from anode to cathode in PEMFC (**Figure 4-9a**). To enhance the device performance, developments of high performance electrocatalyst(*141*, *142*), membrane(*143*, *144*) and novel structure of membrane electrode assembly (MEA)(*145*) have been extensively studied in several decades. Of these, approaches on reducing resistance in Nafion membrane has been explored including lowering thickness of membrane(*146*). However, reducing Nafion thickness in MEA is still challenging and impractical due to the low mechanical properties of Nafion membrane(*33*). We demonstrate here a first trial toward multiscale imprint onto Nafion membrane (**Figure 4-9a, b**). Remarkably, the multiscale Nafion membrane has two distinct structural and physicochemical advantages for the enhanced performance; i) outstandingly elevated surface area for augmenting of triphase boundaries (TPBs) that are region for electrochemical reaction and ii) reduced effective thickness that increases proton conductivity with short transport path.

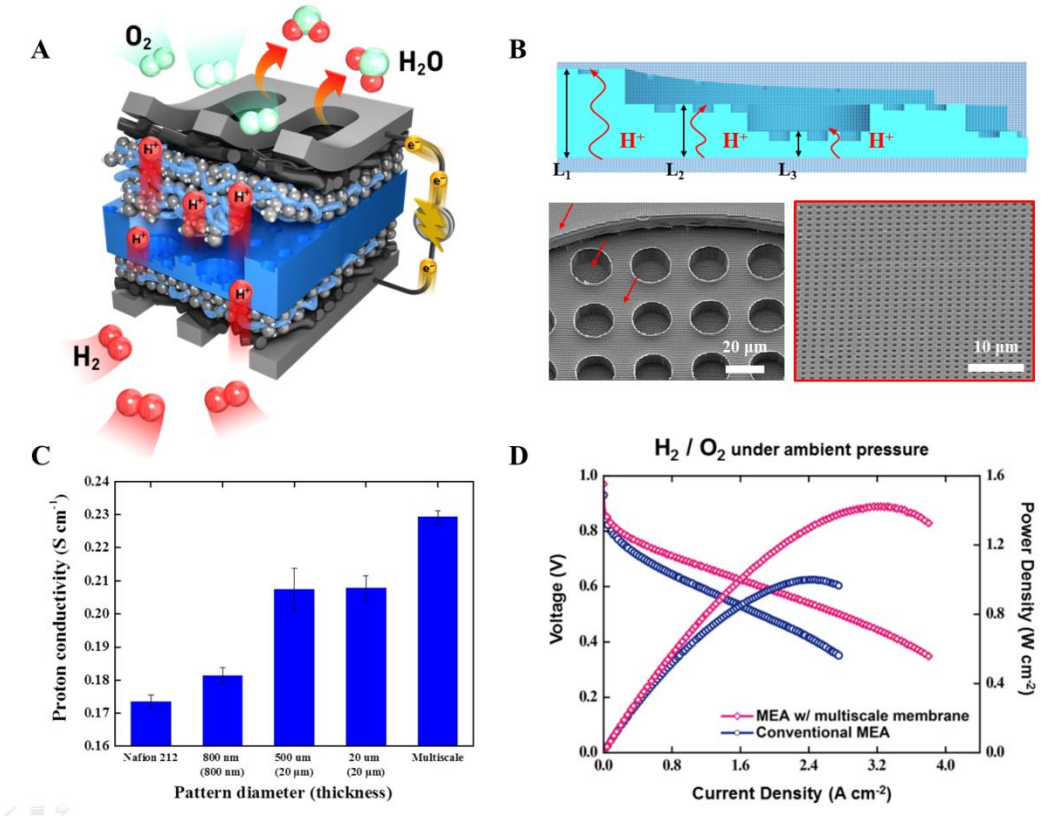

Figure 4-9. Multiscale engineering in polymer electrolyte membrane fuel cell (PEMFC) with complex, hierarchical architectures. (a) Schematic illustration of device operation with multiscale Nafion membrane. (b) Scanning electron microscopy (SEM) images of imprinted multiscale Nafion membrane. (c) Measured proton conductivities of each patterned Nafion membrane. (d) Measured polarization curves for reference membrane electrode assembly (MEA) and MEA with multiscale Nafion membrane in condition of H_2/O_2.

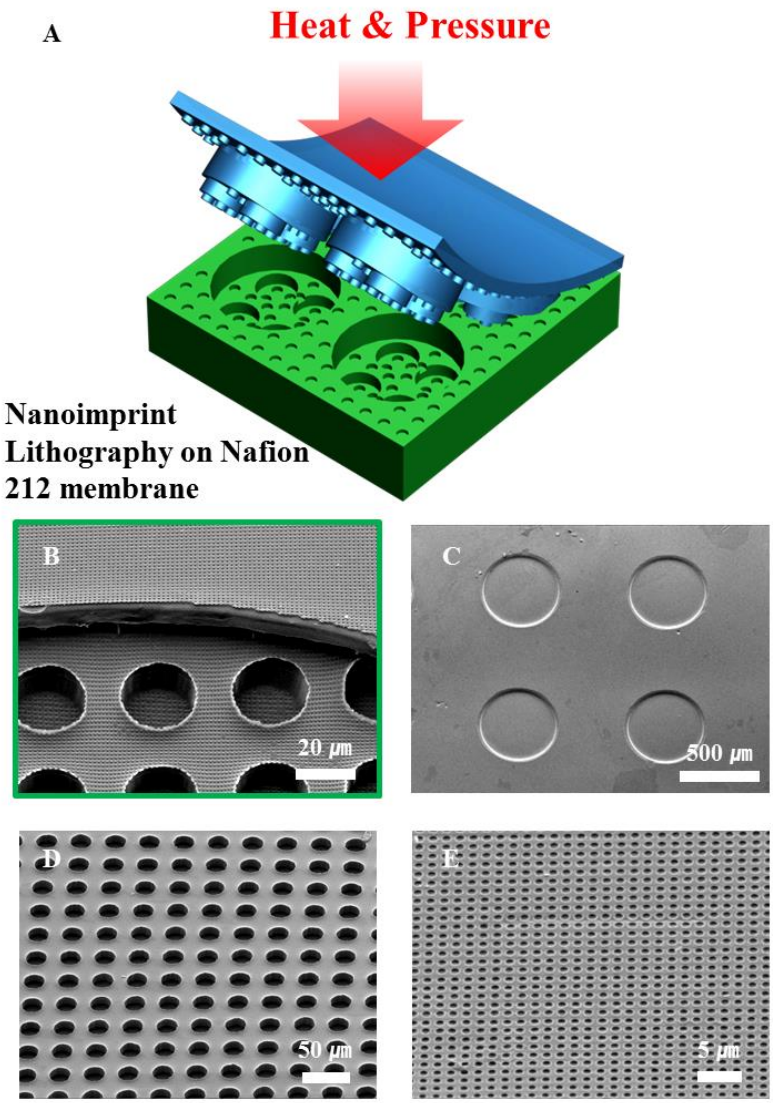

Figure 4-10. (a) Schematic illustration of thermal imprinting process onto Nafion 212 membrane. (b-e) SEM images of patterned Nafion membrane after imprinting process with pattern dimension of multiscale (b), 500 μm (c), 20 μm (d), 800 nm (e).

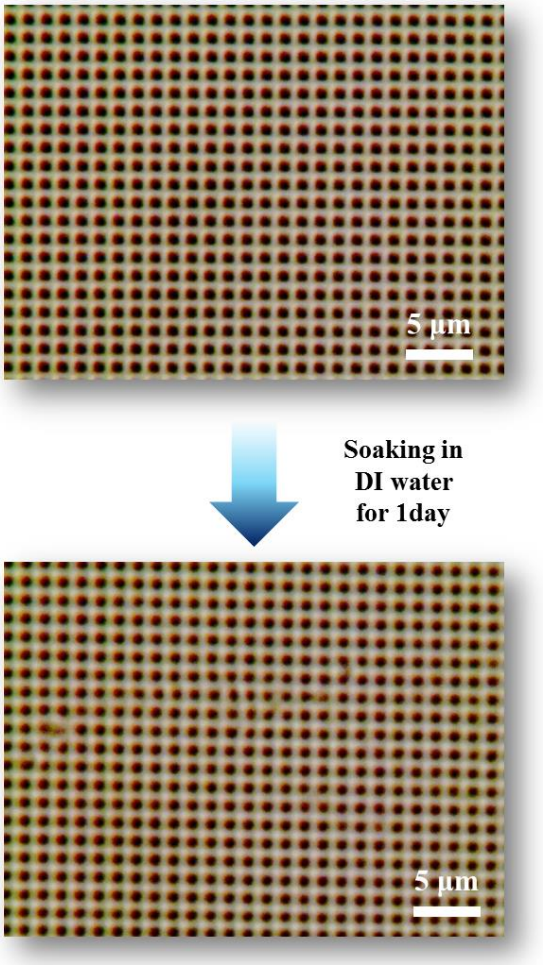

Figure 4-11. Swelling effect of nanopattern-carved nafion membrane after soaking in deionized water for 1day.

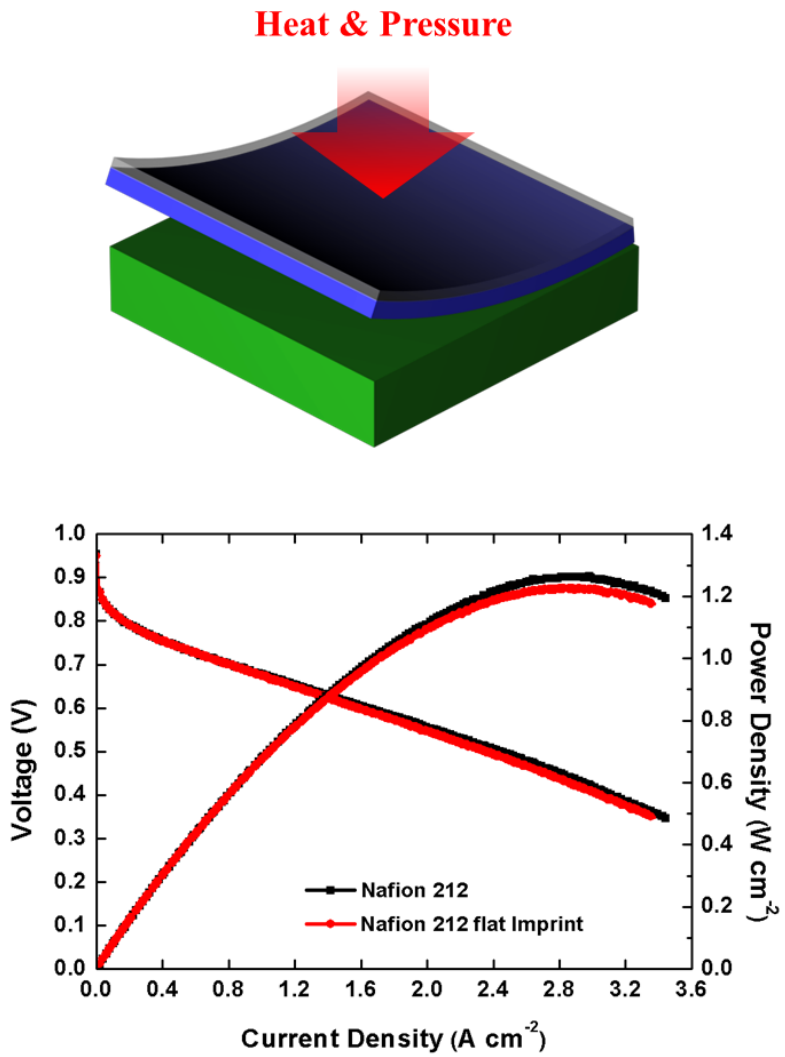

Figure 4-12. Comparison of polarization curves for Nafion membrane with or without hot pressing process(~120℃, 10 kgf cm^{-2}, 10 min) with PDMS (Pt loading: 0.2 mg cm^{-2} in the cathodes and anodes of the MEAs).

Figure 4-9c shows enhanced proton conductivity according to different dimension of patterns on Nafion membrane. In the results, the proton conductivity is inversely proportional to average thickness that is reduced after the imprinting due to the height of carved patterns, where the tri-level architectures (multiscale Nafion membrane) ensured most superior conductivity through hierarchical leveling. Structurally, the multiscale Nafion membrane is consisted with three different thicknesses (L1 > L2 > L3, where L1 is original thickness of membrane (~ 50 μm) (**Figure 4-9a**). As thin Nafion membrane is prone to be fragile during catalyst coating process, the L1 gives a clear geometrical reinforcement by hierarchical leveling to relatively thin areas with a thickness of L2, L3 (*23*). Thereby the both regions (L2, L3) directly affected to the reduced membrane resistance, leading to enhanced performance because the membrane resistance follows ohm's law that is proportional to the distance between two points of conductor. The Nafion membrane was imprinted with good fidelity of original mold as shown in **Figure 4-10**. Furthermore, to check feasibility of nano imprint lithography for Nafion membrane, we conducted experimentals of swelling test of nanopattern-carved nafion membrane after soaking in deionized water for 1day (**Figure 4-11**). The nano patterns on Nafion membrane still remained and were similar with original pattern shapes, so that deformation of original patterns via swelling does not affect seriously in the electrode of MEA. Moreover, heat and pressure during imprint process does not affect the performance of PEMFC as

shown in **Figure 4-12**, so that we confirmed the feasibility of nanoimprint lithography on Nafion membrane. By taking account the structural advantages, we constructed PFMFCs by spraying Pt/C catalysts onto the both sides of membrane. When operating the MEA with multiscale membrane in a condition of fully humidified H_2/O_2, it exhibited outstanding performance compared to a conventional one as shown in the **Figure 4-9d.** It should be noted that MEA with multiscale membrane showed remarkable performance improvement within DOE conditions (*145, 147*). The maximum power density increment of ~42.3% was achieved in case of H_2/O_2 condition under ambient pressure (**Figure 4-9d**). This challenging enhancement is also owing, in part, to the multiscale roughness that enlarge the surface area of Nafion membrane as 1.96 times compared to conventional one as shown in **Figure 4-13**.

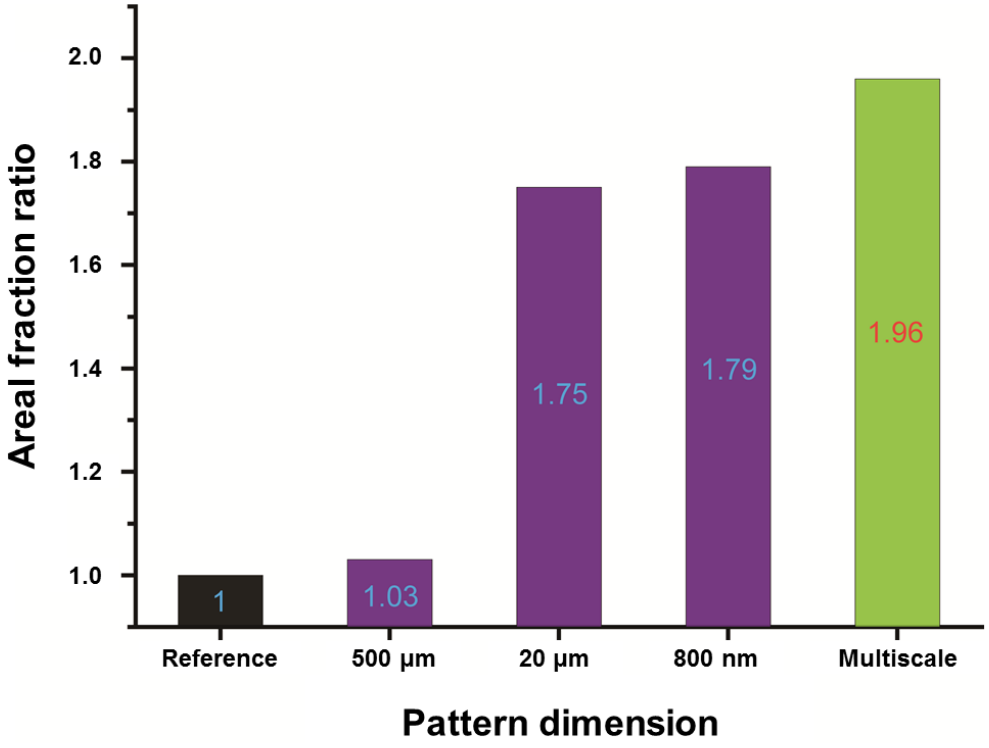

Figure 4-13. Increased surface area ratio compared to flat surface with variation of pattern dimension.

4-2-4. Summary

We have presented a facile yet versatile strategy for multiscale engineering with multiplex lithography. The method involves a series of well-eastabilished procedures including quantitative control of oxygen-inhibition effect to form dual phase bricks from UV-curable polymer and multiplex stacking and curing steps for a LEGO-like deformation. It provides a economically viable route to multiscale engineering by incorporating the multiscale arthitectures into various engineering devices, which takes advantages from each structure in both micro/nanoscale. As remarkable application, multiscale PEMFC was presented with a enhanced proton conductivity, yielding high performance under reliable manners. By taking account the structural advantages, when operating the MEA with multiscale membrane in a condition of fully humidified H_2/O_2 (or H_2/air), it exhibited outstanding performance compared to a conventional one. It should be noted that MEA with multiscale membrane showed remarkable performance improvement within DOE conditions.

References

1. L. Feng, S. Li, Y. Li, H. Li, L. Zhang, J. Zhai, Y. Song, B. Liu, L. Jiang, D. Zhu, Super-hydrophobic surfaces: from natural to artificial. *Advanced materials* **14**, 1857-1860 (2002).
2. Y. Zheng, X. Gao, L. Jiang, Directional adhesion of superhydrophobic butterfly wings. *Soft Matter* **3**, 178-182 (2007).
3. X. Gao, L. Jiang, Biophysics: water-repellent legs of water striders. *Nature* **432**, 36-36 (2004).
4. X. Gao, X. Yan, X. Yao, L. Xu, K. Zhang, J. Zhang, B. Yang, L. Jiang, The Dry-Style Antifogging Properties of Mosquito Compound Eyes and Artificial Analogues Prepared by Soft Lithography. *Advanced Materials* **19**, 2213-2217 (2007).
5. L. Feng, Y. Zhang, J. Xi, Y. Zhu, N. Wang, F. Xia, L. Jiang, Petal effect: a superhydrophobic state with high adhesive force. *Langmuir* **24**, 4114-4119 (2008).
6. K. Liu, X. Yao, L. Jiang, Recent developments in bio-inspired special wettability. *Chemical Society Reviews* **39**, 3240-3255 (2010).
7. Y. Xiu, L. Zhu, D. W. Hess, C. Wong, Hierarchical silicon etched structures for controlled hydrophobicity/superhydrophobicity. *Nano letters* **7**, 3388-3393 (2007).
8. E. Arzt, S. Gorb, R. Spolenak, From micro to nano contacts in biological attachment devices. *Proceedings of the National Academy of Sciences* **100**, 10603-10606 (2003).
9. J. Han, H. Craighead, Separation of long DNA molecules in a microfabricated entropic trap array. *Science* **288**, 1026-1029 (2000).
10. G. Chen, G. T. McCandless, R. L. McCarley, S. A. Soper, Integration of large-area polymer nanopillar arrays into microfluidic devices using in situ polymerization cast molding. *Lab on a Chip* **7**, 1424-1427 (2007).
11. J. O. Tegenfeldt, C. Prinz, H. Cao, R. L. Huang, R. H. Austin, S. Y. Chou, E. C. Cox, J. C. Sturm, Micro-and nanofluidics for DNA analysis. *Analytical and bioanalytical chemistry* **378**, 1678-1692 (2004).
12. H. Cao, J. O. Tegenfeldt, R. H. Austin, S. Y. Chou, Gradient nanostructures for interfacing microfluidics and nanofluidics. *Applied Physics Letters* **81**, 3058-3060 (2002).

13. C. Ye, L. Zhang, X. Fang, Y. Wang, P. Yan, J. Zhao, Hierarchical structure: silicon nanowires standing on silica microwires. *Advanced Materials* **16**, 1019-1023 (2004).
14. Y. T. Tseng, W. H. Tseng, C. H. Lin, R. M. Ho, Fabrication of Double-Length-Scale Patterns via Lithography, Block Copolymer Templating, and Electrodeposition. *Advanced Materials* **19**, 3584-3588 (2007).
15. J. Henzie, M. H. Lee, T. W. Odom, Multiscale patterning of plasmonic metamaterials. *Nature nanotechnology* **2**, 549-554 (2007).
16. A. R. Parker, H. E. Townley, Biomimetics of photonic nanostructures. *Nature Nanotechnology* **2**, 347-353 (2007).
17. M. A. Chong, Y. B. Zheng, H. Gao, L. K. Tan, Combinational template-assisted fabrication of hierarchically ordered nanowire arrays on substrates for device applications. *Applied physics letters* **89**, 233104 (2006).
18. Z. Li, Y. Ding, Y. Xiong, Q. Yang, Y. Xie, One-step solution-based catalytic route to fabricate novel α-MnO 2 hierarchical structures on a large scale. *Chemical communications*, 918-920 (2005).
19. S. Mitragotri, J. Lahann, Physical approaches to biomaterial design. *Nature materials* **8**, 15-23 (2009).
20. L. Gervais, N. De Rooij, E. Delamarche, Microfluidic Chips for Point-of-Care Immunodiagnostics. *Advanced Materials* **23**, H151-H176 (2011).
21. J. El-Ali, P. K. Sorger, K. F. Jensen, Cells on chips. *Nature* **442**, 403-411 (2006).
22. Y. Xia, G. M. Whitesides, Soft lithography. *Annual review of materials science* **28**, 153-184 (1998).
23. H. Cho, J. Kim, H. Park, J. W. Bang, M. S. Hyun, Y. Bae, L. Ha, S. M. Kang, T. J. Park, S. Seo, Replication of flexible polymer membranes with geometry-controllable nano-apertures via a hierarchical mould-based dewetting. *Nature communications* **5**, (2014).
24. W. G. Bae, H. N. Kim, D. Kim, S. H. Park, H. E. Jeong, K. Y. Suh, 25th Anniversary Article: Scalable Multiscale Patterned Structures Inspired by Nature: the Role of Hierarchy. *Advanced Materials* **26**, 675-700 (2014).
25. K. Liu, L. Jiang, Multifunctional integration: from biological to bio-inspired materials. *Acs Nano* **5**, 6786-6790 (2011).
26. H. A. Gasteiger, N. M. Marković, Just a Dream—or Future Reality? *Science* **324**, 48-49

(2009).

27. S. Park, J.-W. Lee, B. N. Popov, A review of gas diffusion layer in PEM fuel cells: materials and designs. *International Journal of Hydrogen Energy* **37**, 5850-5865 (2012).
28. X. Zhang, P. Shi, Dual-bonded catalyst layer structure cathode for PEMFC. *Electrochemistry communications* **8**, 1229-1234 (2006).
29. R. Bashir, BioMEMS: state-of-the-art in detection, opportunities and prospects. *Advanced drug delivery reviews* **56**, 1565-1586 (2004).
30. G. M. Whitesides, The origins and the future of microfluidics. *Nature* **442**, 368-373 (2006).
31. S. M. Kim, B. Lee, H. Yoon, K.-Y. Suh, Stimuli-responsive hydrogel patterns for smart microfluidics and microarrays. *Analyst* **138**, 6230-6242 (2013).
32. P. P. Mukherjee, Q. Kang, C. Y. Wang, Pore-scale modeling of two-phase transport in polymer electrolyte fuel cells—progress and perspective. *Energy Environ. Sci.* **4**, 346-369 (2011).
33. R. P. O'Hayre, S.-W. Cha, W. Colella, F. B. Prinz, Fuel cell fundamentals. (2006).
34. G. M. Whitesides, E. Ostuni, S. Takayama, X. Jiang, D. E. Ingber, Soft lithography in biology and biochemistry. *Annual review of biomedical engineering* **3**, 335-373 (2001).
35. D. Qin, Y. Xia, G. M. Whitesides, Soft lithography for micro-and nanoscale patterning. *Nature protocols* **5**, 491-502 (2010).
36. K.-H. Jeong, J. Kim, L. P. Lee, Biologically inspired artificial compound eyes. *Science* **312**, 557-561 (2006).
37. C. Pang, G.-Y. Lee, T.-i. Kim, S. M. Kim, H. N. Kim, S.-H. Ahn, K.-Y. Suh, A flexible and highly sensitive strain-gauge sensor using reversible interlocking of nanofibres. *Nature materials* **11**, 795-801 (2012).
38. D.-H. Kim, N. Lu, R. Ma, Y.-S. Kim, R.-H. Kim, S. Wang, J. Wu, S. M. Won, H. Tao, A. Islam, Epidermal electronics. *Science* **333**, 838-843 (2011).
39. S. C. Mannsfeld, B. C. Tee, R. M. Stoltenberg, C. V. H. Chen, S. Barman, B. V. Muir, A. N. Sokolov, C. Reese, Z. Bao, Highly sensitive flexible pressure sensors with microstructured rubber dielectric layers. *Nature materials* **9**, 859-864 (2010).
40. R. C. Shallcross, G. S. Chawla, F. S. Marikkar, S. Tolbert, J. Pyun, N. R. Armstrong, Efficient CdSe Nanocrystal Diffraction Gratings Prepared by Microcontact Molding. *ACS*

nano **3**, 3629-3637 (2009).

41. S. A. Morin, R. F. Shepherd, S. W. Kwok, A. A. Stokes, A. Nemiroski, G. M. Whitesides, Camouflage and display for soft machines. *Science* **337**, 828-832 (2012).
42. Y. Xia, E. Kim, X.-M. Zhao, J. A. Rogers, M. Prentiss, G. M. Whitesides, Complex optical surfaces formed by replica molding against elastomeric masters. *Science* **273**, 347-349 (1996).
43. D.-Y. Khang, H. Jiang, Y. Huang, J. A. Rogers, A stretchable form of single-crystal silicon for high-performance electronics on rubber substrates. *Science* **311**, 208-212 (2006).
44. P. Kim, M. Abkarian, H. A. Stone, Hierarchical folding of elastic membranes under biaxial compressive stress. *Nature materials* **10**, 952-957 (2011).
45. W. L. Noorduin, A. Grinthal, L. Mahadevan, J. Aizenberg, Rationally designed complex, hierarchical microarchitectures. *Science* **340**, 832-837 (2013).
46. F. Zhang, J. Chan, H. Y. Low, Biomimetic, hierarchical structures on polymer surfaces by sequential imprinting. *Applied Surface Science* **254**, 2975-2979 (2008).
47. Y. Zhang, C. T. Lin, S. Yang, Fabrication of Hierarchical Pillar Arrays from Thermoplastic and Photosensitive SU-8. *Small* **6**, 768-775 (2010).
48. S. Y. Chou, P. R. Krauss, P. J. Renstrom, 25-nanometer resolution. *Science272*, 85-87 (1996).
49. Y. Hirai, S. Yoshida, N. Takagi, Defect analysis in thermal nanoimprint lithography. *Journal of Vacuum Science & Technology B* **21**, 2765-2770 (2003).
50. H. E. Jeong, R. Kwak, A. Khademhosseini, K. Y. Suh, UV-assisted capillary force lithography for engineering biomimetic multiscale hierarchical structures: from lotus leaf to gecko foot hairs. *Nanoscale* **1**, 331-338 (2009).
51. C. Decker, T. Nguyen Thi Viet, D. Decker, E. Weber-Koehl, UV-radiation curing of acrylate/epoxide systems. *Polymer* **42**, 5531-5541 (2001).
52. J. B. Lambert, H. F. Shurvell, D. A. Lightner, R. G. Cooks, *Introduction to organic spectroscopy*. (Macmillan New York, 1987).
53. S. Tawfick, M. De Volder, D. Copic, S. J. Park, C. R. Oliver, E. S. Polsen, M. J. Roberts, A. J. Hart, Engineering of Micro-and Nanostructured Surfaces with Anisotropic Geometries and Properties. *Advanced Materials* **24**, 1628-1674 (2012).
54. S. M. Kim, J. H. Koh, H. S. Suh, H. Yoon, K.-Y. Suh, K. Char, Thermoresponsive

switching of liquid flow direction on a two-face prism array. *Soft Matter*, (2013).

55. H. Yoon, S.-G. Oh, D. S. Kang, J. M. Park, S. J. Choi, K. Y. Suh, K. Char, H. H. Lee, Arrays of Lucius microprisms for directional allocation of light and autostereoscopic three-dimensional displays. *Nature Communications* **2**, 455 (2011).
56. S.-J. Choi, D. Tahk, H. Yoon, Spontaneous dewetting-induced residue-free patterning at room temperature. *Journal of colloid and interface science* **340**, 74-81 (2009).
57. S.-J. Choi, H. N. Kim, W. G. Bae, K.-Y. Suh, Modulus-and surface energy-tunable ultraviolet-curable polyurethane acrylate: properties and applications. *Journal of Materials Chemistry* **21**, 14325-14335 (2011).
58. S.-J. Choi, K. Y. Suh, H. H. Lee, Direct UV-replica molding of biomimetic hierarchical structure for selective wetting. *Journal of the American Chemical Society* **130**, 6312-6313 (2008).
59. W. G. Bae, S. M. Kim, S. J. Choi, S. G. Oh, H. Yoon, K. Char, K. Y. Suh, In Situ Realization of Asymmetric Ratchet Structures within Microchannels by Directionally Guided Light Transmission and Their Directional Flow Behavior. *Advanced Materials* **26**, 2665-2670 (2014).
60. M. J. Hancock, K. Sekeroglu, M. C. Demirel, Bioinspired directional surfaces for adhesion, wetting, and transport. *Advanced functional materials* **22**, 2223-2234 (2012).
61. D. Xia, L. M. Johnson, G. P. López, Anisotropic Wetting Surfaces with One-Dimesional and Directional Structures: Fabrication Approaches, Wetting Properties and Potential Applications. *Advanced Materials* **24**, 1287-1302 (2012).
62. M. K. Kwak, H.-E. Jeong, T.-i. Kim, H. Yoon, K. Y. Suh, Bio-inspired slanted polymer nanohairs for anisotropic wetting and directional dry adhesion. *Soft Matter* **6**, 1849-1857 (2010).
63. T.-i. Kim, K. Y. Suh, Unidirectional wetting and spreading on stooped polymer nanohairs. *Soft Matter* **5**, 4131-4135 (2009).
64. N. A. Malvadkar, M. J. Hancock, K. Sekeroglu, W. J. Dressick, M. C. Demirel, An engineered anisotropic nanofilm with unidirectional wetting properties. *Nature Materials* **9**, 1023-1028 (2010).
65. K.-H. Chu, R. Xiao, E. N. Wang, Uni-directional liquid spreading on asymmetric nanostructured surfaces. *Nature materials* **9**, 413-417 (2010).

66. V. Jokinen, M. Leinikka, S. Franssila, Microstructured surfaces for directional wetting. *Advanced Materials* **21**, 4835-4838 (2009).
67. L. Kubus, H. Erdogan, E. Piskin, G. Demirel, Controlling uni-directional wetting via surface chemistry and morphology. *Soft Matter* **8**, 11704-11707 (2012).
68. M. P. Murphy, B. Aksak, M. Sitti, Gecko-Inspired Directional and Controllable Adhesion. *Small* **5**, 170-175 (2009).
69. L. F. Boesel, C. Greiner, E. Arzt, A. del Campo, Gecko-Inspired Surfaces: A Path to Strong and Reversible Dry Adhesives. *Advanced Materials* **22**, 2125-2137 (2010).
70. T. Kosako, Y. Kadoya, H. F. Hofmann, Directional control of light by a nano-optical Yagi–Uda antenna. *Nat Photonics* **4**, 312-315 (2010).
71. A. Varley, J. Sule, A. Absalom, Principles of antibiotic therapy. *Continuing Education in Anaesthesia, Critical Care & Pain* **9**, 184-188 (2009).
72. K. B. Neeves, A. A. Onasoga, R. R. Hansen, J. J. Lilly, D. Venckunaite, M. B. Sumner, A. T. Irish, G. Brodsky, M. J. Manco-Johnson, J. A. Di Paola, Sources of Variability in Platelet Accumulation on Type 1 Fibrillar Collagen in Microfluidic Flow Assays. *PloS one* **8**, e54680 (2013).
73. E. Fu, B. Lutz, P. Kauffman, P. Yager, Controlled reagent transport in disposable 2D paper networks. *Lab on a Chip* **10**, 918-920 (2010).
74. C. Extrand, Retention forces of a liquid slug in a rough capillary tube with symmetric or asymmetric features. *Langmuir* **23**, 1867-1871 (2007).
75. A. Palasz, J. Thundathil, R. Verrall, R. Mapletoft, The effect of macromolecular supplementation on the surface tension of TCM-199 and the utilization of growth factors by bovine oocytes and embryos in culture. *Animal reproduction science* **58**, 229-240 (2000).
76. S. Coulson, I. Woodward, J. Badyal, S. Brewer, C. Willis, Ultralow surface energy plasma polymer films. *Chemistry of materials* **12**, 2031-2038 (2000).
77. J. Oliver, C. Huh, S. Mason, Resistance to spreading of liquids by sharp edges. *Journal of Colloid and Interface Science* **59**, 568-581 (1977).
78. F.-M. Chang, S.-J. Hong, Y.-J. Sheng, H.-K. Tsao, Wetting invasion and retreat across a corner boundary. *The Journal of Physical Chemistry C* **114**, 1615-1621 (2010).
79. V. Liimatainen, V. Sariola, Q. Zhou, Controlling Liquid Spreading Using Microfabricated

Undercut Edges. *Advanced Materials*, (2013).

80. O. Sandre, L. Gorre-Talini, A. Ajdari, J. Prost, P. Silberzan, Moving droplets on asymmetrically structured surfaces. *Physical Review E* **60**, 2964 (1999).
81. H. Kusumaatmaja, C. Pooley, S. Girardo, D. Pisignano, J. Yeomans, Capillary filling in patterned channels. *Physical Review E* **77**, 067301 (2008).
82. H. Kusumaatmaja, J. Yeomans, Anisotropic hysteresis on ratcheted superhydrophobic surfaces. *Soft Matter* **5**, 2704-2707 (2009).
83. A. W. Martinez, S. T. Phillips, Z. Nie, C.-M. Cheng, E. Carrilho, B. J. Wiley, G. M. Whitesides, Programmable diagnostic devices made from paper and tape. *Lab on a Chip* **10**, 2499-2504 (2010).
84. J. P. Rolland, D. A. Mourey, Paper as a novel material platform for devices. *MRS Bulletin* **38**, 299-305 (2013).
85. P. Kim, H.-Y. Kim, J. K. Kim, G. Reiter, K. Y. Suh, Multi-curvature liquid meniscus in a nanochannel: Evidence of interplay between intermolecular and surface forces. *Lab on a Chip* **9**, 3255-3260 (2009).
86. G. Lagubeau, M. Le Merrer, C. Clanet, D. Quéré, Leidenfrost on a ratchet. *Nature Physics* **7**, 395-398 (2011).
87. D. Zhang, F. Chen, Q. Yang, J. Si, X. Hou, Mutual wetting transition between isotropic and anisotropic on directional structures fabricated by femotosecond laser. *Soft Matter* **7**, 8337-8342 (2011).
88. S.-G. Park, J. H. Moon, H. C. Jeon, S.-M. Yang, Anisotropic wetting and superhydrophobicity on holographically featured 3D nanostructured surfaces. *Soft Matter* **8**, 4567-4570 (2012).
89. S. Daniel, S. Sircar, J. Gliem, M. K. Chaudhury, Ratcheting motion of liquid drops on gradient surfaces. *Langmuir* **20**, 4085-4092 (2004).
90. Y. Zheng, H. Bai, Z. Huang, X. Tian, F.-Q. Nie, Y. Zhao, J. Zhai, L. Jiang, Directional water collection on wetted spider silk. *Nature* **463**, 640-643 (2010).
91. J. Ju, H. Bai, Y. Zheng, T. Zhao, R. Fang, L. Jiang, A multi-structural and multi-functional integrated fog collection system in cactus. *Nature communications* **3**, 1247 (2012).
92. M. Prakash, D. Quéré, J. W. Bush, Surface tension transport of prey by feeding shorebirds: the capillary ratchet. *science* **320**, 931-934 (2008).

93. H. S. Khoo, F.-G. Tseng, Spontaneous high-speed transport of subnanoliter water droplet on gradient nanotextured surfaces. *Applied Physics Letters* **95**, 063108 (2009).

94. L. Courbin, E. Denieul, E. Dressaire, M. Roper, A. Ajdari, H. A. Stone, Imbibition by polygonal spreading on microdecorated surfaces. *Nature materials* **6**, 661-664 (2007).

95. P. Papadopoulos, X. Deng, L. Mammen, D.-M. Drotlef, G. Battagliarin, C. Li, K. Müllen, K. Landfester, A. del Campo, H.-J. r. Butt, Wetting on the microscale: shape of a liquid drop on a microstructured surface at different length scales. *Langmuir* **28**, 8392-8398 (2012).

96. H. Bai, J. Ju, R. Sun, Y. Chen, Y. Zheng, L. Jiang, Controlled fabrication and water collection ability of bioinspired artificial spider silks. *Advanced Materials* **23**, 3708-3711 (2011).

97. X. Liu, Q. Ye, X. Song, Y. Zhu, X. Cao, Y. Liang, F. Zhou, Responsive wetting transition on superhydrophobic surfaces with sparsely grafted polymer brushes. *Soft Matter* **7**, 515-523 (2011).

98. J. Kim, J. A. Hanna, R. C. Hayward, C. D. Santangelo, Thermally responsive rolling of thin gel strips with discrete variations in swelling. *Soft Matter* **8**, 2375-2381 (2012).

99. G. Stoychev, N. Puretskiy, L. Ionov, Self-folding all-polymer thermoresponsive microcapsules. *Soft Matter* **7**, 3277-3279 (2011).

100. T. Sun, G. Wang, L. Feng, B. Liu, Y. Ma, L. Jiang, D. Zhu, Reversible switching between superhydrophilicity and superhydrophobicity. *Angewandte Chemie International Edition* **43**, 357-360 (2004).

101. F. Xia, L. Feng, S. Wang, T. Sun, W. Song, W. Jiang, L. Jiang, Dual-Responsive Surfaces That Switch between Superhydrophilicity and Superhydrophobicity. *Advanced Materials* **18**, 432-436 (2006).

102. F. Xia, L. Jiang, Bio-Inspired, Smart, Multiscale Interfacial Materials. *Advanced materials* **20**, 2842-2858 (2008).

103. H. Tekin, T. Tsinman, J. G. Sanchez, B. J. Jones, G. Camci-Unal, J. W. Nichol, R. Langer, A. Khademhosseini, Responsive micromolds for sequential patterning of hydrogel microstructures. *Journal of the American Chemical Society* **133**, 12944-12947 (2011).

104. H. Tekin, M. Anaya, M. D. Brigham, C. Nauman, R. Langer, A. Khademhosseini, Stimuli-responsive microwells for formation and retrieval of cell aggregates. *Lab on a*

Chip **10**, 2411-2418 (2010).

105. X. Zhu, G. Wu, R. Dong, C.-M. Chen, S. Yang, Capillarity induced instability in responsive hydrogel membranes with periodic hole array. *Soft Matter* **8**, 8088-8093 (2012).

106. M. Han, C. Xu, D. Zhu, L. Yang, J. Zhang, Y. Chen, K. Ding, F. Song, G. Wang, Controllable Synthesis of Two-Dimensional Metal Nanoparticle Arrays with Oriented Size and Number Density Gradients. *Advanced Materials* **19**, 2979-2983 (2007).

107. P. Yu, C. H. Chang, C. H. Chiu, C. S. Yang, J. C. Yu, H. C. Kuo, S. H. Hsu, Y. C. Chang, Efficiency enhancement of GaAs photovoltaics employing antireflective indium tin oxide nanocolumns. *Advanced Materials* **21**, 1618-1621 (2009).

108. N. Li, S. R. Forrest, Tilted bulk heterojunction organic photovoltaic cells grown by oblique angle deposition. *Applied Physics Letters* **95**, 123309 (2009).

109. Y. Choi, S. Hong, L. P. Lee, Shadow overlap ion-beam lithography for nanoarchitectures. *Nano letters* **9**, 3726-3731 (2009).

110. H. Yoon, H. E. Jeong, T.-i. Kim, T. J. Kang, D. Tahk, K. Char, K. Y. Suh, Adhesion hysteresis of Janus nanopillars fabricated by nanomolding and oblique metal deposition. *Nano Today* **4**, 385-392 (2009).

111. N. Jung, S. M. Kim, D. H. Kang, D. Y. Chung, Y. S. Kang, Y.-H. Chung, Y. W. Choi, C. Pang, K.-Y. Suh, Y.-E. Sung, High-Performance Hybrid Catalyst with Selectively Functionalized Carbon by Temperature-Directed Switchable Polymer. *Chemistry of Materials* **25**, 1526-1532 (2013).

112. H. Li, Y. Tang, Z. Wang, Z. Shi, S. Wu, D. Song, J. Zhang, K. Fatih, H. Wang, A review of water flooding issues in the proton exchange membrane fuel cell. *Journal of Power Sources* **178**, 103-117 (2008).

113. I. E. L. Stephens, A. S. Bondarenko, U. Grønbjerg, J. Rossmeisl, I. Chorkendorff, Understanding the electrocatalysis of oxygen reduction on platinum and its alloys. *Energy & Environmental Science*, (2012).

114. P. K. Sinha, P. P. Mukherjee, C. Y. Wang, Impact of GDL structure and wettability on water management in polymer electrolyte fuel cells. *J. Mater. Chem.* **17**, 3089-3103 (2007).

115. D. Wang, C. V. Subban, H. Wang, E. Rus, F. J. DiSalvo, H. D. Abruña, Highly Stable and

CO-Tolerant Pt/Ti0. 7W0. 3O2 Electrocatalyst for Proton-Exchange Membrane Fuel Cells. *Journal of the American Chemical Society*, (2010).

116. M. Uchida, Y. Aoyama, N. Eda, A. Ohta, Investigation of the Microstructure in the Catalyst Layer and Effects of Both Perfluorosulfonate Ionomer and PTFE-Loaded Carbon on the Catalyst Layer of Polymer Electrolyte Fuel Cells. *Journal of the Electrochemical Society* **142**, 4143 (1995).
117. R. Friedmann, T. Van Nguyen, Optimization of the Microstructure of the Cathode Catalyst Layer of a PEMFC for Two-Phase Flow. *Journal of the Electrochemical Society* **157**, B260 (2010).
118. J. Zhao, X. He, L. Wang, J. Tian, C. Wan, C. Jiang, Addition of NH< sub> 4</sub> HCO< sub> 3</sub> as pore-former in membrane electrode assembly for PEMFC. *International Journal of Hydrogen Energy* **32**, 380-384 (2007).
119. Y. Song, Y. Wei, H. Xu, M. Williams, Y. Liu, L. J. Bonville, H. Russell Kunz, J. M. Fenton, Improvement in high temperature proton exchange membrane fuel cells cathode performance with ammonium carbonate. *Journal of Power Sources* **141**, 250-257 (2005).
120. N. Jung, Y. H. Cho, M. Ahn, J. W. Lim, Y. S. Kang, D. Y. Chung, J. Kim, Y. E. Sung, Methanol-tolerant cathode electrode structure composed of heterogeneous composites to overcome methanol crossover effects for direct methanol fuel cell. *International Journal of Hydrogen Energy*, (2011).
121. T. V. Reshetenko, H. T. Kim, H. J. Kweon, Cathode structure optimization for air-breathing DMFC by application of pore-forming agents. *Journal of Power Sources* **171**, 433-440 (2007).
122. X. Yu, S. Ye, Recent advances in activity and durability enhancement of Pt/C catalytic cathode in PEMFC:: Part II: Degradation mechanism and durability enhancement of carbon supported platinum catalyst. *Journal of Power Sources* **172**, 145-154 (2007).
123. Y. Xing, Synthesis and electrochemical characterization of uniformly-dispersed high loading Pt nanoparticles on sonochemically-treated carbon nanotubes. *The Journal of Physical Chemistry B* **108**, 19255-19259 (2004).
124. H. S. Oh, H. Kim, Efficient Synthesis of Pt Nanoparticles Supported on Hydrophobic Graphitized Carbon Nanofibers for Electrocatalysts Using Noncovalent Functionalization. *Advanced Functional Materials*, (2011).

125. J. Chen, Q. Chen, Q. Ma, Influence of surface functionalization via chemical oxidation on the properties of carbon nanotubes. *Journal of Colloid and Interface Science* **370**, 32-38 (2012).

126. N. Jung, Y. H. Cho, K. H. Choi, J. W. Lim, M. Ahn, Y. S. Kang, Y. E. Sung, Preparation process for improving cathode electrode structure in direct methanol fuel cell. *Electrochemistry communications* **12**, 754-757 (2010).

127. M. Ebara, M. Yamato, T. Aoyagi, A. Kikuchi, K. Sakai, T. Okano, Temperature-responsive cell culture surfaces enable "on-off" affinity control between cell integrins and RGDS ligands. *Biomacromolecules* **5**, 505-510 (2004).

128. G. Huang, J. Gao, Z. Hu, J. V. St John, B. C. Ponder, D. Moro, Controlled drug release from hydrogel nanoparticle networks. *Journal of controlled release* **94**, 303-311 (2004).

129. S. Zhu, C. Chen, Z. Chen, X. Liu, Y. Li, Y. Shi, D. Zhang, Thermo-responsive polymer-functionalized mesoporous carbon for controlled drug release. *Materials Chemistry and Physics* **126**, 357-363 (2011).

130. X. Zhang, C. L. Pint, M. H. Lee, B. E. Schubert, A. Jamshidi, K. Takei, H. Ko, A. Gillies, R. Bardhan, J. J. Urban, Optically-and thermally-responsive programmable materials based on carbon nanotube-hydrogel polymer composites. *Nano letters*, (2011).

131. N. I. Abu-Lail, M. Kaholek, B. LaMattina, R. L. Clark, S. Zauscher, Micro-cantilevers with end-grafted stimulus-responsive polymer brushes for actuation and sensing. *Sensors and Actuators B: Chemical* **114**, 371-378 (2006).

132. M. Ben-Moshe, V. L. Alexeev, S. A. Asher, Fast responsive crystalline colloidal array photonic crystal glucose sensors. *Analytical chemistry* **78**, 5149-5157 (2006).

133. G. R. Hendrickson, L. A. Lyon, Bioresponsive hydrogels for sensing applications. *Soft Matter* **5**, 29-35 (2009).

134. N. Nakajima, Y. Ikada, Mechanism of amide formation by carbodiimide for bioconjugation in aqueous media. *Bioconjugate chemistry* **6**, 123-130 (1995).

135. B. Ruelle, S. Peeterbroeck, R. Gouttebaron, T. Godfroid, F. Monteverde, J. P. Dauchot, M. Alexandre, M. Hecq, P. Dubois, Functionalization of carbon nanotubes by atomic nitrogen formed in a microwave plasma Ar+ N2 and subsequent poly (ε-caprolactone) grafting. *J. Mater. Chem.* **17**, 157-159 (2006).

136. Q. Peng, X. He, Y. Li, C. Wang, R. Wang, P. A. Hu, Y. Yan, T. Sritharan, Chemically and

uniformly grafting carbon nanotubes onto carbon fibers by poly (amidoamine) for enhancing interfacial strength in carbon fiber composites. *Journal of Materials Chemistry*, (2012).

137. E. Chibowski, Surface free energy of a solid from contact angle hysteresis. *Advances in colloid and interface science* **103**, 149-172 (2003).
138. Y. Rahmawan, M. W. Moon, K. S. Kim, K. R. Lee, K. Y. Suh, Wrinkled, dual-scale structures of diamond-like carbon (DLC) for superhydrophobicity. *Langmuir* **26**, 484-491 (2009).
139. J. Benziger, J. Nehlsen, D. Blackwell, T. Brennan, J. Itescu, Water flow in the gas diffusion layer of PEM fuel cells. *Journal of membrane science* **261**, 98-106 (2005).
140. J. N. Israelachvili, *Intermolecular and surface forces*. (Academic press, 2011).
141. C. Chen, Y. Kang, Z. Huo, Z. Zhu, W. Huang, H. L. Xin, J. D. Snyder, D. Li, J. A. Herron, M. Mavrikakis, Highly crystalline multimetallic nanoframes with three-dimensional electrocatalytic surfaces. *Science* **343**, 1339-1343 (2014).
142. G. Wu, K. L. More, P. Xu, H.-L. Wang, M. Ferrandon, A. J. Kropf, D. J. Myers, S. Ma, C. M. Johnston, P. Zelenay, A carbon-nanotube-supported graphene-rich non-precious metal oxygen reduction catalyst with enhanced performance durability. *Chemical Communications* **49**, 3291-3293 (2013).
143. J. W. Bae, Y.-H. Cho, Y.-E. Sung, K. Shin, J. Y. Jho, Performance enhancement of polymer electrolyte membrane fuel cell by employing line-patterned Nafion membrane. *Journal of Industrial and Engineering Chemistry* **18**, 876-879 (2012).
144. J. K. Koh, Y. Jeon, Y. I. Cho, J. H. Kim, Y.-G. Shul, A facile preparation method of surface patterned polymer electrolyte membranes for fuel cell applications. *Journal of Materials Chemistry A* **2**, 8652-8659 (2014).
145. O.-H. Kim, Y.-H. Cho, S. H. Kang, H.-Y. Park, M. Kim, J. W. Lim, D. Y. Chung, M. J. Lee, H. Choe, Y.-E. Sung, Ordered macroporous platinum electrode and enhanced mass transfer in fuel cells using inverse opal structure. *Nature communications* **4**, (2013).
146. S. Slade, S. Campbell, T. Ralph, F. Walsh, Ionic conductivity of an extruded Nafion 1100 EW series of membranes. *Journal of The Electrochemical Society* **149**, A1556-A1564 (2002).
147. C. Houchins, G. J. Kleen, J. S. Spendelow, J. Kopasz, D. Peterson, N. L. Garland, D. L.

Ho, J. Marcinkoski, K. E. Martin, R. Tyler, US DOE progress towards developing low-cost, high performance, durable polymer electrolyte membranes for fuel cell applications. *Membranes* **2**, 855-878 (2012).

국 문 초 록

본 학위 논문에서는 자외선 경화 고분자의 부분경화 현상 및 특정 광학 필름을 이용해 빛의 방향성을 조절함으로써 자외선 경화 고분자로 구성된 멀티스케일 혹은 비대칭 구조물을 제작하기 위한 새롭고 용이한 공정을 제시하고 있다. 또한, 열 감응성 고분자를 자연모사 멀티스케일 구조물에 적용하여, 마이크로 유체 시스템에서의 일방향성 액체 흐름 조절을 구현하였으며, 수소연료전지 (고분자 전해질막 연료전지) 시스템에 적용하여 성능을 향상시킨 결과를 제시하였다.

먼저, 자연계 생물체 표면에 존재하는 멀티스케일 구조물을 모사하기 위한 새롭고 용이한 리소그래피에 대해 소개하였다. 대표적으로, 자외선 경화 고분자의 부분경화 현상을 이용하여 마이크로 고분자 막을 제작하여, 이를 적층시켜가며 각 층의 패턴의 치수와 층의 개수를 설계 및 제작할 수 있는 멀티플렉스 리소그래피를 제시하였다. 마이크로 고분자 막은 산소 투과 효과 및 비젖음 특성을 이용하여 제작이 되며, 마이크로 고분자 막 표면에 남아있는 액적은 추가 자외선 조사를 통해 나노 패턴을 새기거나 두 개의 마이크로 고분자 막을 연결하는 역할을 하게 된다. 이에 더해, 몰포나비 날개 혹은 소금쟁이 다리의 멀티스케일, 비대칭 래칫 구조물을 모사하기 위한 간단하면서도 유용한 제작 공법을 제시하였다. 마이크로 채널 내에 자외선 경화 고분자를 채워넣은 상태에서 UV 빛을 특정 각도로 휘게 만들어 주는

루시우스 프리즘 어레이 를 통과시켜 마이크로 채널 내에 직접적으로 비대칭 래칫 구조물을 형성하였다.

다음으로, 마이크로 채널 내에 형성된 멀티스케일, 비대칭 구조물을 이용하여 마이크로 유체 시스템 내에서의 일방향성 유체 흐름 특성 구현 및 래칫 구조물의 방향성을 조절하여 특정 구역에서의 유체 속도 조절 가능성을 확인하였다. 비대칭 래칫 구조물을 이용하여 외부 펌프 및 밸브 장치가 없이 마이크로 유체 시스템에서의 속도 조절 및 유체 흐름 지연을 통한 타이머의 응용을 보여주었다. 또한, 구조적으로 대칭의 특성을 지니는 고분자 프리즘 어레이에 기울임 금속 증착 공법을 적용하여 물리적으로 대칭이지만 화학적으로 비대칭인 프리즘 어레이를 제작하여 일방향성 젖음 특성을 구현하였다. 이에 더해, 특정 자극에 따라 유체 흐름의 방향성을 바꾸고자 프리즘 어레이를 구성하는 고분자를 저온(< 32 ℃)에서 친수 성질을, 고온(> 32 ℃)에서는 소수 성질을 나타내는 열감응성 고분자(poly(N-isopropylacrylamide))를 이용해 패터닝하여, 온도에 따라서 유체 흐름을 바꿀 수 있는 마이크로 유체 시스템을 개발하였다.

마지막으로, 열감응성 고분자(poly(N-isopropylacrylamide))를 탄소 나노입자의 표면에 선택적으로 개질하여 수소 연료 전지 음극에서 발생하는 물의 이동을 촉진시켜 전지의 효율이 향상됨을 규명하였다. 기존 방법들의 경우, 고분자가 촉매(Platinum; Pt) 표면을 감싸 활성 면적을 줄이거나 두께를 증가시켜 산소 확산을 저하시켜 성능을

저하시켰다. 본 연구에서는 Amine($-NH_2$) 작용기가 달려 있는 열감응성 고분자를 Pt/C 촉매에 대해 Pt 에 영향을 주지 않으면서도 탄소 표면에만 선택적으로 개질시킨 후, 저온에서 친수 성질을 띄게 하여 촉매 분산의 문제를 없애고, 수소연료전지 운전시(~ 70 ℃)에 소수 성질을 가지게 하여 물을 효율적으로 배출시켜 물질 전달 증가에 의한 수소연료전지 성능 향상을 유도하였다. 또한 모델링을 통해 물 전달 정도를 상대적으로 비교할 수 있는 지수(index)를 제시하였다. 이에 더해, 멀티플렉스 리소그래피 공정을 통해 제작된 멀티스케일 고분자 구조물을 나노임프린트 리소그래피 공정을 통해 이온교환막에 계층구조물을 새긴 후, 이를 막-전극 접합체에 도입하였다. 이를 통해 막 두께를 감소시켜 수소이온의 전도를 용이하게 하고, 이온교환막의 표면의 구조물로 인한 전극 표면적의 증가를 유도하여 수소연료전지의 성능을 향상시키는 효과를 가져왔다.

주요어: 멀티스케일 구조물, 비대칭 구조물, 자외선 경화 고분자, 열감응성 고분자, 방향성 유체 흐름, 고성능 수소연료전지

학번: 2010-22782